Article

Cell Reports

Targeting EGLN2/PHD1 protects motor neurons and normalizes the astrocytic interferon response

Graphical abstract

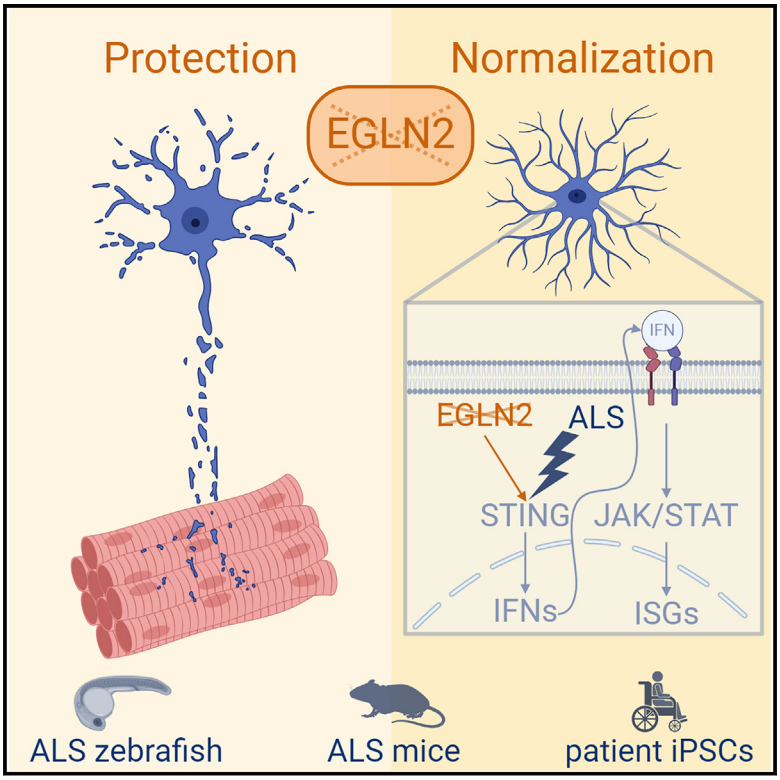

Authors

Christine Germeys, Tijs Vandoorne, Kristofer Davie, ..., Philip Van Damme, Katrien De Bock, Ludo Van Den Bosch

Correspondence

ludo.vandenbosch@kuleuven.be

In brief

Germeys et al. identify EGLN2 as an ALS target that, when downregulated, protects motor neurons and mitigates the ALS phenotype in ALS zebrafish and mice. Using snRNA-seq and CRISPR-Cas9-edited patient iPSCs, they show that the downregulation of EGLN2 normalizes the STING-induced astrocytic interferon response *in vivo* and in patient-derived cells.

Highlights

- *Egln2* knockdown rescues motor axonopathy in both C9- and SOD1-ALS zebrafish
- *Egln2* deletion mitigates ALS phenotypes in SOD1-ALS mice and prolongs survival
- *EGLN2* deletion normalizes STING-induced interferon response in ALS astrocytes

Germeys et al., 2024, Cell Reports *43*, 114719
September 24, 2024
https://doi.org/10.1016/j.celrep.2024.114719

CellPress

Cell Reports

CellPress
OPEN ACCESS

Article

Targeting EGLN2/PHD1 protects motor neurons and normalizes the astrocytic interferon response

Christine Germeys,[1,2,17] Tijs Vandoorne,[1,2,17] Kristofer Davie,[3] Suresh Poovathingal,[4,5] Kara Heeren,[1,2] Wendy Vermeire,[1,2] FatemehArefeh Nami,[6] Matthieu Moisse,[1,2] Annelies Quaegebeur,[7,8] Annerieke Sierksma,[9,10] Laura Rué,[1,2] Adrià Sicart,[1,2] Caroline Eykens,[1,2] Lenja De Cock,[1,2] Bart De Strooper,[9,10,11] Peter Carmeliet,[12,13,14] Philip Van Damme,[1,2,15] Katrien De Bock,[16,18] and Ludo Van Den Bosch[1,2,18,19,*]

[1]KU Leuven – University of Leuven, Department of Neurosciences, Experimental Neurology and Leuven Brain Institute (LBI), 3000 Leuven, Belgium
[2]VIB, Center for Brain & Disease Research, Laboratory of Neurobiology, 3000 Leuven, Belgium
[3]VIB-KU Leuven, Center for Brain & Disease Research Technologies, Single Cell Bioinformatics Unit, 3000 Leuven, Belgium
[4]VIB-KU Leuven, Center for Brain & Disease Research Technologies, Single Cell Microfluidics & Analytics Unit, 3000 Leuven, Belgium
[5]VIB, Center for AI & Computational Biology (VIB.AI), 3000 Leuven, Belgium
[6]KU Leuven – University of Leuven, Department of Development and Regeneration, Stem Cell Institute Leuven (SCIL), 3000 Leuven, Belgium
[7]University of Cambridge, Department of Clinical Neurosciences, CB2 2PY Cambridge, UK
[8]Cambridge University Hospitals, Department of Histopathology, CB2 0QQ Cambridge, UK
[9]KU Leuven – University of Leuven, Department of Neurosciences, Research Group Molecular Neurobiology and Leuven Brain Institute (LBI), 3000 Leuven, Belgium
[10]VIB, Center for Brain & Disease Research, Laboratory for the Research of Neurodegenerative Diseases, 3000 Leuven, Belgium
[11]Dementia Research Institute, University College London, WC1E 6BT London, UK
[12]KU Leuven – University of Leuven, Department of Oncology and Leuven Cancer Institute (LKI), Laboratory of Angiogenesis and Vascular Metabolism, 3000 Leuven, Belgium
[13]VIB, Center for Cancer Biology, Laboratory of Angiogenesis and Vascular Metabolism, 3000 Leuven, Belgium
[14]Khalifa University of Science and Technology, Center for Biotechnology, Abu Dhabi, United Arab Emirates
[15]University Hospitals Leuven, Department of Neurology, 3000 Leuven, Belgium
[16]ETH Zürich, Department of Health Sciences and Technology, 8092 Zürich, Switzerland
[17]These authors contributed equally
[18]These authors contributed equally
[19]Lead contact
*Correspondence: ludo.vandenbosch@kuleuven.be
https://doi.org/10.1016/j.celrep.2024.114719

SUMMARY

Neuroinflammation and dysregulated energy metabolism are linked to motor neuron degeneration in amyotrophic lateral sclerosis (ALS). The egl-9 family hypoxia-inducible factor (EGLN) enzymes, also known as prolyl hydroxylase domain (PHD) enzymes, are metabolic sensors regulating cellular inflammation and metabolism. Using an oligonucleotide-based and a genetic approach, we showed that the downregulation of *Egln2* protected motor neurons and mitigated the ALS phenotype in two zebrafish models and a mouse model of ALS. Single-nucleus RNA sequencing of the murine spinal cord revealed that the loss of EGLN2 induced an astrocyte-specific downregulation of interferon-stimulated genes, mediated via the stimulator of interferon genes (STING) protein. In addition, we found that the genetic deletion of *EGLN2* restored this interferon response in patient induced pluripotent stem cell (iPSC)-derived astrocytes, confirming the link between EGLN2 and astrocytic interferon signaling. In conclusion, we identified EGLN2 as a motor neuron protective target normalizing the astrocytic interferon-dependent inflammatory axis *in vivo*, as well as in patient-derived cells.

INTRODUCTION

The egl-9 family hypoxia-inducible factor (EGLN) enzymes EGLN1, -2, and -3, also known as prolyl hydroxylase domain (PHD)-containing enzymes PHD2, -1, and -3, respectively, are oxygen sensors and master regulators of the response to hypoxia.[1] Next to oxygen, α-ketoglutarate, ferrous iron (Fe^{2+}), and ascorbic acid are also required co-factors, while other tricarboxylic acid cycle intermediates inhibit EGLN activity.[2–4] As a result, EGLNs also function as metabolic sensors and can respond accordingly via a range of cell- and context-specific targets.[5] The canonical target of the EGLN enzymes is hypoxia-inducible factor (HIF)α.[6,7] During normoxia, EGLN enzymes target HIFα for proteasomal degradation through hydroxylation. Under hypoxic conditions, EGLN enzymes lose their ability to hydroxylate HIF, which leads to HIF stabilization and the transcription of HIF targets that play a role in a variety of pathways, including cellular metabolism.[8] Interestingly, genetic ablation of the EGLN2

enzyme has been shown to protect skeletal muscle[9] and hepatocytes[10] against oxidative stress via the activation of a HIF transcriptomic response. Moreover, the downregulation of EGLN2 protected cortical neurons against oxidative stress in models for stroke through metabolic rewiring independent from HIF.[11] In addition, IκB kinase (IKKβ) is a well-known HIF-independent target of EGLN2.[12] As a result, EGLN2 regulates, via IKKβ, the activity of the nuclear factor kappa-light-chain-enhancer of activated B cells (NF-κB) pathway, playing a central role in the cellular inflammatory response.[11–13]

Oxidative stress, metabolic dysfunction, and neuroinflammation are hallmarks of amyotrophic lateral sclerosis (ALS),[14] a fatal neurodegenerative disorder characterized by the degeneration of upper and lower motor neurons in the motor cortex, brainstem, and spinal cord. Signs of elevated levels of oxidative stress are found in postmortem brain and spinal cord tissue from patients with sporadic ALS.[15,16] Also, defects in energy metabolism, the main cellular source of reactive oxygen species (ROS),[17] are well known in ALS models and patients with ALS and correlate with disease progression in the latter.[18,19] Interestingly, compounds that provide protection against hypoxic stress, via the induction of a HIF1α transcriptional response, increased the survival of ALS mice.[20,21] Moreover, HIF-induced transcription of vascular endothelial growth factor (VEGF) has also been shown to be involved in motor neuron survival,[22] and the delivery of VEGF *in vivo* and *in vitro* provides protection against motor neuron degeneration.[23,24] In addition to the metabolic defects, neuroinflammation also plays a crucial role in ALS pathology. The neuroinflammatory response in ALS, characterized by microglial and astroglial activation, T lymphocyte infiltration, and elevated levels of pro-inflammatory cytokines,[25] is shown to be present in models and patients[26–28] and correlates with disease progression in the latter.[29] Moreover, an increase in the activation of NF-κB has been observed in astrocytes and microglia from patients with ALS and ALS models.[30,31] Besides its role in energy metabolism,[9–11] EGLN2 also plays a central role in NF-κB signaling,[11–13] making EGLN2 a unique target that is involved in the cellular regulation of two of the main hallmarks of ALS.

In this study, we showed that the downregulation of *Egln2* mitigated motor neuron degeneration in transgenic mouse and zebrafish models of ALS. Single-nucleus RNA sequencing (snRNA-seq) of the spinal cord of early symptomatic ALS mice revealed that the loss of EGLN2 induced a downregulation of stimulator of interferon genes (STING)-induced gene expression in astrocytes. This link between EGLN2 and the astrocytic interferon response was strengthened by our finding that in patient induced pluripotent stem cell (iPSC)-derived astrocytes, the ablation of EGLN2 also restored the levels of interferon-stimulated genes. Therefore, we propose EGLN2 as an ALS target protecting motor neurons in different *in vivo* models for ALS and describe a link between EGLN2 and astrocytic interferon signaling.

RESULTS

Downregulation of *egln2* rescues the motor axonopathy in ALS zebrafish

To explore the role of EGLN2 in ALS, we targeted Egln2 in two ALS zebrafish models. These zebrafish models, in which we injected human mutant *SOD1*^{G93A} (SOD1^{G93A}) and 91 copies of *C9orf72* sense repeat (91S) RNA, develop a motor axonopathy with a decreased axonal length and an increased percentage of abnormally branched axons (Figures 1C–1E, S1A, and S1B). The downregulation of *egln2* was achieved by injecting an antisense oligonucleotide morpholino (AMO) that targets the exon 2/intron 2 splice junction of *egln2*, resulting in the removal of exon 2 (Figures 1A and 1B) without affecting the mRNA levels of *egln1a* and *-b* and *egln3* (Figures S1C–S1E). Co-injection with the *egln2* AMO in both SOD1^{G93A} and 91S zebrafish almost completely rescued the motor axon abnormalities, increasing the axonal length and decreasing the abnormal branching of the motor axons (Figures 1C–1E, S1A, and S1B). Lemmens et al. previously demonstrated that the upregulation of Vegf could rescue the motor axonopathy induced by mutant *SOD1*.[32] However, the *egln2* AMO did not affect the expression of *vegfaa* (Figure S1F) in SOD1^{G93A} zebrafish, suggesting that the motor neuron protective effect is independent from this Hif target. These results demonstrated how targeting Egln2, using an oligonucleotide-based approach, protects motor neurons in a C9 and SOD1 *in vivo* model for ALS.

Deletion of *Egln2* prolongs survival and mitigates motor neuron degeneration in SOD1^{G93A} mice

To investigate whether targeting EGLN2 also protects motor neurons in a more complex model system for ALS, we crossed *Egln2* knockout mice (*Egln2*$^{-/-}$)[33] with ALS mice expressing mutant human SOD1^{G93A}.[34] *Egln2* mRNA expression in the spinal cord was reduced by 55% in *SOD1*^{G93A}/*Egln2*$^{+/-}$ compared to *SOD1*^{G93A}/*Egln2*$^{+/+}$ mice and was not detectable in *SOD1*^{G93A}/*Egln2*$^{-/-}$ mice (Figure S2A). Deletion of *Egln2* did not cause any compensatory upregulation of *Egln1* or *Egln3* at the mRNA level (Figures S2B and S2C), nor did it affect human SOD1 expression in the spinal cord of SOD1^{G93A} mice (Figure S2D). The age at disease onset, defined by a reduction in body weight of 10% and reduced rotarod performance, was not altered by the deletion of *Egln2* (Figures 2A and 2B). However, homozygous, but not heterozygous, deletion of *Egln2* significantly prolonged the mean survival of SOD1^{G93A} mice from 147 ± 2 days for *SOD1*^{G93A}/*Egln2*$^{+/+}$ mice to 157 ± 3 days for *SOD1*^{G93A}/*Egln2*$^{-/-}$ mice (Figure 2C). As a result, disease duration, defined as the number of days between disease onset and the humane endpoint, increased by 44% in *SOD1*^{G93A}/*Egln2*$^{-/-}$ mice (Figure 2D).

To investigate whether the observed survival benefit was linked to a mitigation of motor neuron degeneration, we quantified the neurons in the ventral horn of early symptomatic mice at 110 days of age (post-natal day [P]110). The number of remaining neurons in the ventral horn of *SOD1*^{G93A}/*Egln2*$^{-/-}$ mice was higher compared to *SOD1*^{G93A}/*Egln2*$^{+/+}$ mice (Figures 2E and 2F). This neuroprotective effect was more pronounced for large motor neurons (>400 μm^2: +63%) compared to smaller neurons (250–400 μm^2: +44%, 150–200 μm^2: +47%, 200–250 μm^2: +48%) (Figures 2E and 2F). To investigate whether the loss of EGLN2 also protected neuromuscular junction (NMJ) innervation, we quantified this in the gastrocnemius muscle at P110. Innervation of the NMJs in the gastrocnemius muscle was better preserved in *SOD1*^{G93A}/*Egln2*$^{-/-}$ mice compared

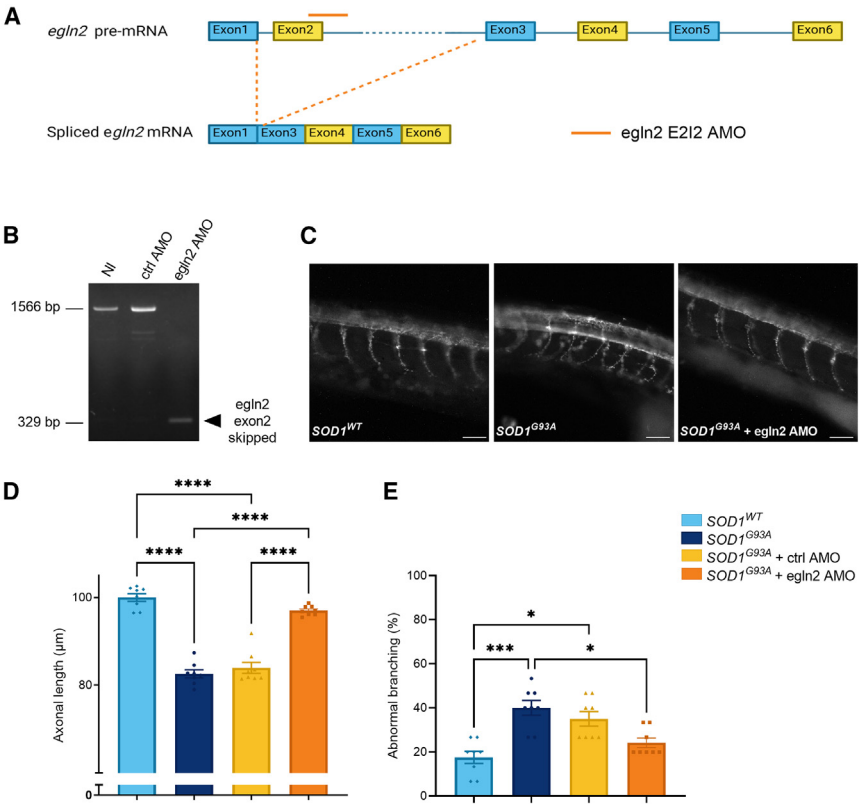

Figure 1. *Egln2* downregulation rescues motor axonopathy in SOD1^{G93A} zebrafish

(A) Schematic representation of the splice-block antisense oligonucleotide morpholino (AMO) that targets the exon 2-intron 2 (E2I2) junction in zebrafish *egln2* pre-mRNA, resulting in a differentially spliced *egln2*.

(B) Validation of the AMO-induced splice defect using RT-PCR. Wild-type (WT) *egln2* cDNA in 30 h post-fertilization (hpf) non-injected (NI) and control (ctrl) AMO or alternative splice product induced by E2I2 splice-blocking AMO, indicated by the arrowhead.

(C) Representative images of synaptic vesicle glycoprotein 2a (SV2) staining at 30 hpf in zebrafish injected with *SOD1^{WT}* RNA, *SOD1^{G93A}* RNA, and *SOD1^{G93A}* RNA with *egln2* AMO. Scale bar, 50 µm.

(D) Quantification of the axonal length.

(E) Quantification of the percentage of abnormally branched axons.

Data represent mean ± SEM with individual values shown (N = 8 experiments, each with 15 zebrafish per group). Statistical analyses were performed in (D) by a one-way ANOVA with Sidak's multiple comparison test and in (E) with the Kruskal-Wallis test with Dunn's multiple comparison test ($^{*}p < 0.05$, $^{***}p < 0.001$, and $^{****}p < 0.0001$).

to *SOD1^{G93A}/Egln2$^{+/+}$* mice (Figure 2G). Together, these results showed that the loss of EGLN2 mitigated motor neuron degeneration in early symptomatic SOD1^{G93A} mice. In addition, this was observed in the absence of changes in blood vessel density or an effect on the expression level of HIF target genes in lumbar spinal cord tissue (Figures S2E–S2G), suggesting that the motor neuron protective effect of *Egln2* deletion in SOD1^{G93A} mice, in line with the zebrafish data, was independent from these HIF targets.

Overall, these data indicate that knocking out *Egln2* has a positive effect on the ALS phenotype of the SOD1^{G93A} mouse model, slowing down the disease progression, increasing motor neuron survival, and increasing muscle innervation.

Egln2 deletion induces a decrease in astrocytic interferon signaling in SOD1^{G93A} spinal cord

To gain insight into the cell-specific pathways underlying the beneficial effect of *Egln2* downregulation, we performed snRNA-seq on the lumbar spinal cord of P110 *SOD1^{G93A}/Egln2$^{+/+}$* and *SOD1^{G93A}/Egln2$^{-/-}$* mice. We transcriptionally profiled a total of 42,278 nuclei (quality control; Table S1) and identified 35 distinct nucleus clusters accounting for the different neuronal and non-neuronal cell types present in the murine spinal cord (Figure 3; Table S2). Cluster 35 (in purple) was identified as the motor neuron cluster, as this cluster specifically expressed known motor neuron markers[35–43] (*Slc18a3*, *Slc5a7*, *Nefl*, *Nefm*, *Nefh*, *Uchl1*, *Ubb*, *Prph*), including *Stmn2*,[44,45] which was confirmed to co-localize specifically with large synaptophysin-positive neurons in the ventral horn of the lumbar spinal cord using RNAscope *in situ* hybridization[44,45] (Figure S3; Table S2). All clusters, including the motor neuron cluster, contained nuclei of all six samples (Figure S4), which allowed us to study the effect of *Egln2* deletion on cluster-specific gene expression.

Differentially expressed gene (DEG) analysis on all 35 clusters revealed an overall total of 724 upregulated DEGs and 1,653 downregulated DEGs in *SOD1^{G93A}/Egln2$^{-/-}$* versus *SOD1^{G93A}/Egln2$^{+/+}$* clusters (Table S3). Gene Ontology (GO) enrichment analysis of the up- and downregulated DEGs revealed that the deletion of *Egln2* induced a transcriptomic change in a range of biological processes in neuronal and non-neuronal cells (Table 1). In the motor neuron cluster, genes related to synapse organization, ion transport, neurogenesis, and cell adhesion were downregulated upon loss of EGLN2 (Table 1). While these included a number of genes that were linked to ALS before,[46–51] no potential mechanism of action emerged. Interestingly, we also observed a downregulation of the translocator protein (*Tspo*)[52] (Table S3), which has been proposed as a biomarker for neuroinflammation.[53] Because of their central role in ALS-linked neuroinflammation,[25] we next focused on the microglia and astrocytes. While GO analysis did not detect any biologically relevant effect of *Egln2$^{-/-}$* on inflammatory pathways in microglia, we did observe a downregulation of interferon-stimulated genes in the *SOD1^{G93A}/Egln2$^{-/-}$* astrocyte cluster marked by several known astrocyte markers[54] (including *Aqp4*, *Aldh1l1*, *Gfap*, *Agt*, *Apoe*, *Glul*, *Slc1a3*, and *Aldoc*) (Figure 4A). This type of response can be provoked by the GMP-AMP synthase (cGAS)/STING pathway, regulating the innate immune response

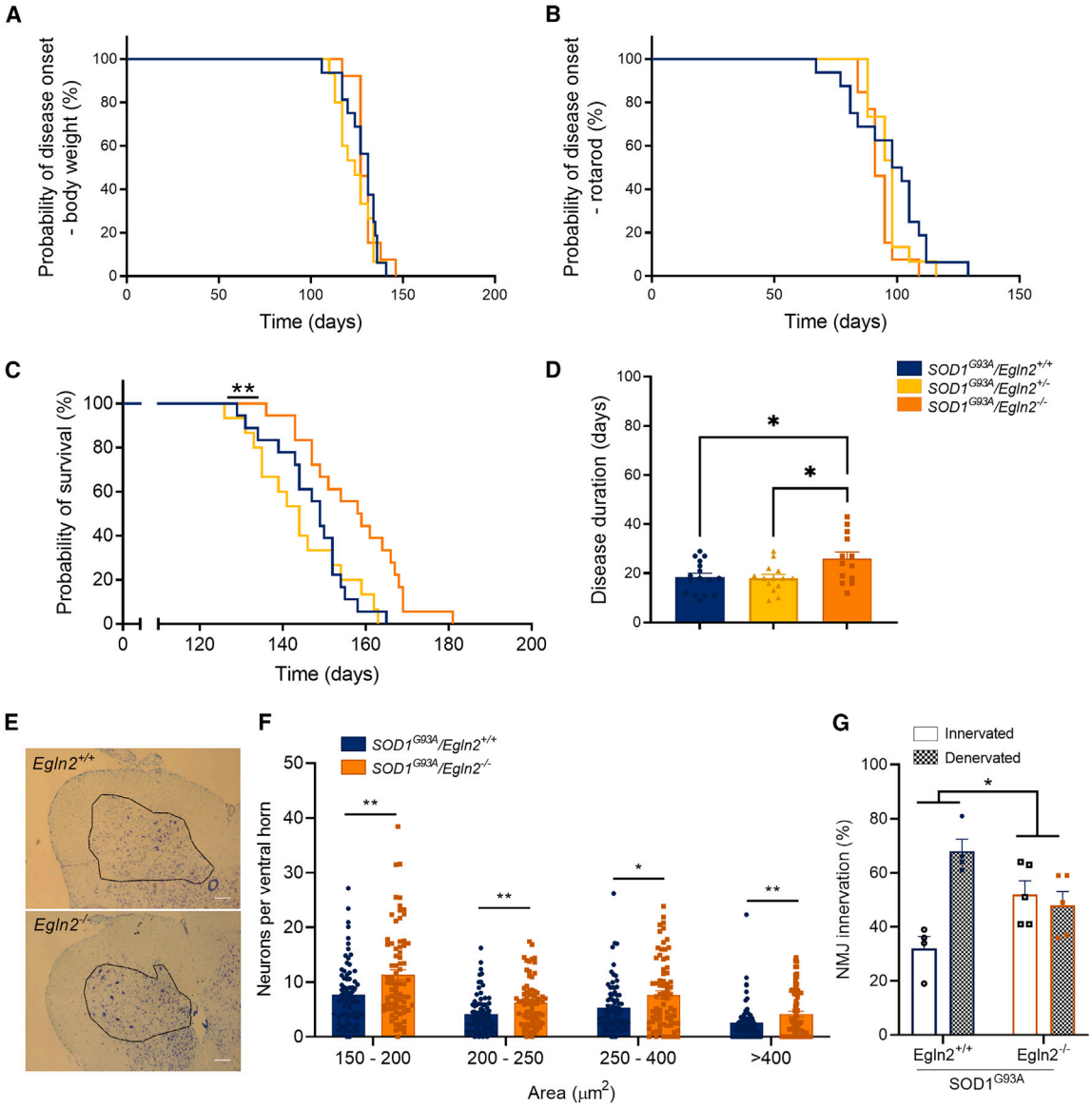

Figure 2. *Egln2* deletion prolongs survival and mitigates motor neuron degeneration in SOD1^{G93A} mice

(A) Probability of disease onset assessed by a body weight reduction of 10%. *SOD1^{G93A}/Egln2$^{+/+}$* $N = 16$, *SOD1^{G93A}/Egln2$^{+/-}$* $N = 15$, and *SOD1^{G93A}/Egln2$^{-/-}$* $N = 13$.

(B) Probability of disease onset assessed by a reduction of the performance time on the rotarod below 150 s. *SOD1^{G93A}/Egln2$^{+/+}$* $N = 16$, *SOD1^{G93A}/Egln2$^{+/-}$* $N = 15$, and *SOD1^{G93A}/Egln2$^{-/-}$* $N = 13$.

(C) Probability of survival; humane endpoint defined as loss of righting reflex within 20 s. *SOD1^{G93A}/Egln2$^{+/+}$* $N = 18$, SOD1^{G93A}/*Egln2$^{+/-}$* $N = 15$, and *SOD1^{G93A}/Egln2$^{-/-}$* $N = 18$.

(D) Disease duration defined as days between disease onset and humane endpoint. *SOD1^{G93A}/Egln2$^{+/+}$* $N = 16$, *SOD1^{G93A}/Egln2$^{+/-}$* $N = 15$, and *SOD1^{G93A}/Egln2$^{-/-}$* $N = 13$.

(E) Representative thionin staining of neurons in the lumbar spinal cord of *SOD1^{G93A}/Egln2$^{+/+}$* and *SOD1^{G93A}/Egln2$^{-/-}$* mice at P110. Ventral horn indicated in black. Scale bar, 150 μm.

(F) Quantification of number of neurons in the ventral horn of *SOD1^{G93A}/Egln2$^{+/+}$* and *SOD1^{G93A}/Egln2$^{-/-}$* mice normalized to 300,000 μm^2 of ventral horn and categorized per size.

(G) Percentages of innervated and denervated neuromuscular junctions (NMJs) in *SOD1^{G93A}/Egln2$^{+/+}$* and *SOD1^{G93A}/Egln2$^{-/-}$* mice at P110.

Data represent mean ± SEM with individual values shown ($N \geq 4$ mice per group). Statistical analyses were performed in (A)–(C) by log-rank Mantel-Cox, in (D) by a one-way ANOVA with Tukey's multiple comparison, in (F) by a two-way ANOVA with Sidak's multiple comparison test, and in (G) by an unpaired t test (*$p < 0.05$ and **$p < 0.01$).

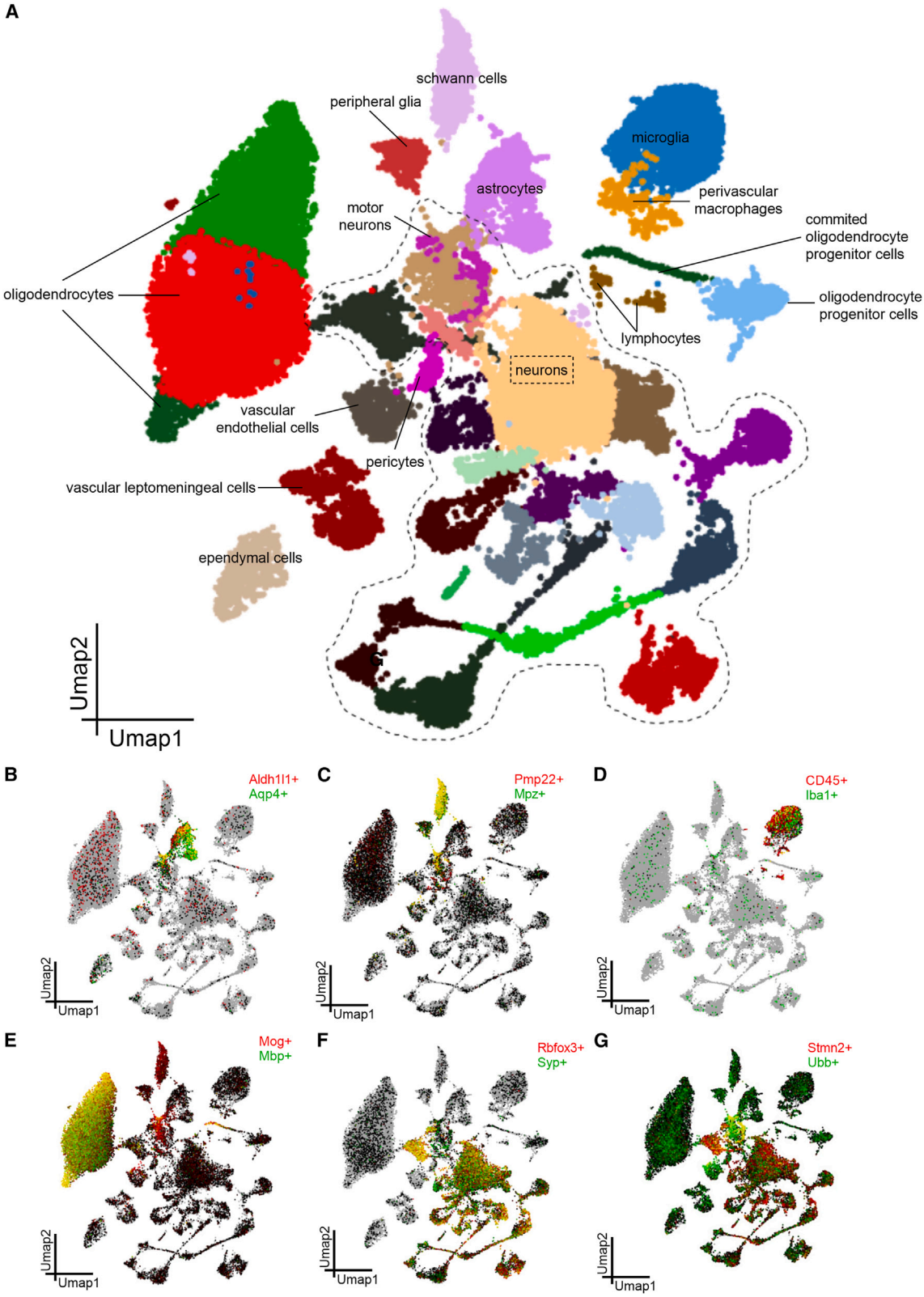

(legend on next page)

to cytosolic double-stranded DNA (dsDNA), resulting in the canonical activation through TANK-binding kinase 1 (TBK1) and interferon regulatory factor 3 (IRF3) or non-canonical NF-κB activation (Figure 4B). Gene set enrichment analysis (GSEA) suggested that the expression of these genes was reduced via the canonical cGAS/STING pathway and not via a reduction of NF-κB activation, which even showed a trend toward enrichment in the upregulated gene set of *SOD1*^{G93A}/*Egln2*$^{-/-}$ astrocytes (Figure 4C). While not reaching significance in the GSEA, we observed a reduction in STING protein expression, marking decreased cGAS/STING pathway activation, in glial fibrillary acidic protein (GFAP)-positive cells of the ventral horn of *SOD1*^{G93A}/*Egln2*$^{-/-}$ mice compared to *SOD1*^{G93A}/*Egln2*$^{+/+}$ mice (Figures 4D and 4E).

As a result, these data showed that the deletion of *Egln2* reduced the expression of neuroinflammation marker *Tspo* in motor neurons while at the same time decreasing the cGAS/STING-induced pro-inflammatory interferon response in astrocytes, suggesting that *Egln2* deletion reduces the astrocytic interferon-dependent inflammatory axis.

EGLN2 deletion normalizes the expression of interferon-stimulated genes in ALS patient-derived astrocytes

To further explore the direct effect of loss of EGLN2 on astrocytes from patients with ALS, *EGLN2* was deleted in iPSCs derived from a patient with ALS carrying a *SOD1*^{A4V} mutation[57] using CRISPR-Cas9 (Figure S5). To study the effect of loss of *EGLN2* on patient-derived astrocytes, we differentiated *SOD1*^{A4V}/*EGLN2*$^{-/-}$ and *SOD1*^{A4V} iPSCs together with isogenic control (*SOD1*^{A4A}) iPSCs, which were genetically corrected for the *SOD1*^{A4V} mutation,[57] into astrocytes (Figures 5A and S6A). RNA-seq analysis revealed that the transcriptome of *SOD1*^{A4V}/*EGLN2*$^{-/-}$ astrocytes was more similar to the transcriptome of isogenic *SOD1*^{A4A} astrocytes compared to *SOD1*^{A4V} astrocytes (Figure S6B), indicating that *EGLN2* deletion rescued ALS-induced defects in these cells. To identify the pathways that are rescued upon loss of *EGLN2* in astrocytes, DEG analyses between the different astrocyte lines were performed (Table S4). 676 genes were differentially expressed in both *SOD1*^{A4V} versus *SOD1*^{A4A} astrocytes and *SOD1*^{A4V}/*EGLN2*$^{-/-}$ versus *SOD1*^{A4V} astrocytes (Figure 5B). From these 676 overlapping DEGs, 511 DEGs were downregulated in *SOD1*^{A4V} versus *SOD1*^{A4A} astrocytes and upregulated in *SOD1*^{A4V}/*EGLN2*$^{-/-}$ versus *SOD1*^{A4V} astrocytes (Figure 5C), indicating that the expression of these genes was rescued upon loss of EGLN2. This gene set mainly included genes linked to the interferon response, including the ones that were found to be downregulated in the snRNA-seq analysis (Figure 5D). As a result, this showed that in monocultured patient astrocytes, *EGLN2* deletion increased the expression of interferon-stimulated genes, while these were downregulated in astrocytes from *SOD1*^{G93A}/*Egln2*$^{-/-}$ mice. Moreover, GSEA suggested that the effect of *EGLN2* knockout on the interferon response could be driven by an activation of the canonical cGAS/STING-TBK1-IRF3 and non-canonical NF-κB pathways (Figure 5E).

The interferon response plays a crucial role in pro-inflammatory signaling, and while astrogliosis and microgliosis are present in SOD1^{G93A} mice at P110,[58] this is not the case in these human astrocyte monocultures (Figure 6A). To investigate whether the lack of neuroinflammatory stimuli could explain the difference in the effects on the interferon genes, we provoked an inflammatory response, marked by the previously described markers,[59] in our iPSC-derived astrocytes by treatment with a pro-inflammatory microglia-derived cocktail of tumor necrosis factor alpha (TNF-α), interleukin (IL)-1α, and C1q (TIC)[60] (Figure 6A). *SOD1*^{A4V} astrocytes showed a greater transcriptional response to the TIC treatment compared to *SOD1*^{A4A} (Figure 6B) and *SOD1*^{A4V}/*EGLN2*$^{-/-}$ astrocytes (Figure 6C). Remarkably, the latter two showed a similar response to the TIC treatment, as no differences in the gene expression affected by the treatment were observed between *SOD1*^{A4A} and *SOD1*^{A4V}/*EGLN2*$^{-/-}$ astrocytes (Figure 6D). Following the same approach as described above to identify the pathways that are rescued by *EGLN2* knockout (Figures 6E and 6F), we found that *SOD1*^{A4V} astrocytes still expressed lower levels of interferon-stimulated genes after treatment with the TIC cocktail, which could again be rescued by the loss of EGLN2 (Figures 6G; Table S4). Finally, we also compared the differences in expression levels of interferon-stimulated genes between *SOD1*^{A4V} and *SOD1*^{A4A} astrocytes to publicly available ALS patient-derived astrocyte RNA-seq datasets.[61–65] However, we did not find a clear overlap between the expression patterns (Table S5).

In conclusion, we showed that *SOD1*^{A4V}ALS patient-derived astrocytes present an altered interferon-dependent inflammatory response and that this response could be rescued by the deletion of *EGLN2*, supporting the link between EGLN2 and the astrocytic interferon response. As a result, our study highlights EGLN2 as a potential ALS target that protects motor neurons and normalizes the interferon response in ALS astrocytes.

DISCUSSION

In this study, we identified EGLN2 as motor neuron protective target using several *in vivo* ALS models, snRNA-seq, and patient-derived iPSCs. We showed that targeting *egln2* using an AMO in both SOD1-and C9-ALS zebrafish protected the motor neurons, leading to a rescue of ALS-induced motor axonopathy. Moreover, in a more complex model of ALS, the SOD1^{G93A} mouse model, genetic deletion of *Egln2* also mitigated the ALS phenotype by protecting motor neurons and prolonging survival. snRNA-seq revealed that the loss of EGLN2 induced an

Figure 3. Single-nucleus transcriptomics reveals neuronal and non-neuronal cell clusters in SOD1^{G93A} spinal cord

(A) Uniform manifold approximation and projection (UMAP) plot visualizing 42,278 nuclei isolated from the lumbar spinal cord of P110 *SOD1*^{G93A}/*Egln2*$^{+/+}$ and *SOD1*^{G93A}/*Egln2*$^{-/-}$ mice. *SOD1*^{G93A}/*Egln2*$^{+/+}$ *N* = 3 and *SOD1*^{G93A}/*Egln2*$^{-/-}$ *N* = 3. The annotation of different clusters is based on publicly available transcriptomics data.

(B–G) Individual nuclei colored by expression for classical markers for (B) astrocytes, (C) Schwann cells, (D) microglia, (E) myelinating oligodendrocytes, (F) neurons, and (G) motor neurons using SCope.

Table 1. GO analysis on DEGs from *SOD1*^{G93A}/*Egln2*$^{-/-}$ versus *SOD1*^{G93A}/*Egln2*$^{+/+}$ lumbar spinal cord at P110

Biological process	GO term	Cell type	Top 5 DEGs
Upregulated			
Immune/defense response	GO: 0042119; GO: 0036230; GO: 0031349; GO: 0031347	excitatory neurons	*Mmp12*, *Syk*, *Anxa1*, *Serping1*, *Ctss*
Synapse assembly	GO: 0007416; GO: 0034329; GO: 0034330; GO: 0050808	perivascular macrophages	*Ctnna2*, *Nrxn3*, *Adgrl3*, *Lrrtm4*, *Nrg1*
Action potential	GO: 0001508	perivascular macrophages	*Grik2*, *Kcnc2*, *Dpp6*, *Dmd*, *Cntnap2*
Cell adhesion	GO: 0098742; GO: 0098609; GO: 0007155; GO: 0022610	perivascular macrophages	*Robo2*, *Ctnna2*, *Tenm2*, *Nrxn3*, *Ninj1*
Translation	GO: 0002181	motor neurons	*Rpl30*, *Rps15*, *Rpl28*, *Rpl37a*, *Rpl22L1*
Downregulated			
Synapse assembly/ transmission	GO: 0048167; GO: 0050804; GO: 0099177; GO: 0007268; GO: 0098916; GO: 0099537; GO: 0099536	myelinating oligodendrocytes	*Glra2*, *Kcnh1*, *Sv2b*, *Akap12*, *Erc2*
Synapse assembly/ transmission	GO: 0099558; GO: 0034331; GO: 0050808; GO: 0034330; GO: 0060078; GO: 0042391; GO: 0007416; GO: 0034329; GO: 0051966; GO: 0050804; GO: 0099177; GO: 0007268; GO: 0098916; GO: 0099537; GO: 0099536; GO: 0050807; GO: 0050803; GO: 1901890	peripheral glial cells	*Arhgap6*, *Syn1*, *Rgs7*, *Fgf13*, *Slc4a4*
Synapse assembly/ transmission	GO: 0051963	lymphocytes	*Adgrb3*, *Mdga2*, *Negr1*, *Grid2*
Synapse assembly/ transmission	GO: 1905606; GO: 0099174; GO: 1901888; GO: 0050807; GO: 0050803; GO: 0007416; GO: 0034329; GO: 0034330; GO: 0050808; GO: 0051965; GO: 1901890; GO: 0051962; GO: 0051960; GO: 0050804; GO: 0099177; GO: 0042391	motor neurons	*Dcc*, *Grik2*, *Nrg3*, *Nrp1*, *Fxyd1*
Ion transport	GO: 0043269; GO: 0034762	myelinating oligodendrocytes	*Kcnh1*, *Ano6*, *Kcnip4*, *Kcnc2*, *Jph3*
Ion transport	GO: 0032412; GO: 0022898; GO: 0032409; GO: 0034762; GO: 0034765; GO: 0043269; GO: 1904062	peripheral glial cells	*Kcnh1*, *Ano6*, *Kcnip4*, *Kcnc2*, *Jph3*
Ion transport	GO: 1904062; GO: 0034765	motor neurons	*Asic2*, *Fxyd1*, *Pde4d*, *Dpp10*, *Dmd*
Oxidative metabolism	GO: 0006091; GO: 0006119; GO: 0006754; GO: 0009060; GO: 0009141; GO: 0009142; GO: 0009145; GO: 0009199; GO: 0009201; GO: 0009205; GO: 0009206; GO: 0015980; GO: 0015986; GO: 0019646; GO: 0022900; GO: 0022904; GO: 0042773; GO: 0042775; GO: 0042776; GO: 0045333; GO: 0046034	neurons	*Slc1a3*, *Ndufa7*, *Hspa8*, *S100b*, *Uqcr11*
Viral response	GO: 0045071; GO: 0045069; GO: 1903900; GO: 0050792; GO: 0048525; GO: 0051607; GO: 0009615; GO: 0140546	astrocytes	*Cxcl10*, *Oasl1*, *Isg15*, *Rsad2*, *Ifit1*
Cell death	GO: 0042981; GO: 0043067; GO: 0010941	astrocytes	*Cxcl10*, *Igfbp3*, *Ier3*, *Fcgr2b*, *Rac3*
Cell death	GO: 1902255; GO: 1901798; GO: 0010942	neurons	*Tac1*, *Unc13b*, *Rps15*, *Snca*, *Rpl26*
Translation	GO: 0002181; GO: 0006412; GO: 0043043; GO: 0043604; GO: 0006518; GO: 0043603; GO: 0034645; GO: 0008016; GO: 0044271; GO: 1901566	neurons	*Vdr*, *Galnt5*, *Mlycd*, *Mrpl49*, *S100a10*
Action potential	GO: 0001508	peripheral glial cells	*Cacna1c*, *Grin2b*, *Gria1*, *Kcnd2*, *Cntnap2*

(*Continued on next page*)

Table 1. *Continued*

Biological process	GO term	Cell type	Top 5 DEGs
Neurogenesis	GO: 0051962; GO: 0051960; GO: 0048812; GO: 0120039; GO: 0048858; GO: 0031175; GO: 0048666; GO: 0030182; GO: 0048699; GO: 0022008; GO: 0048667; GO: 0007420; GO: 0007417; GO: 0010975; GO: 0120035; GO: 0031344	peripheral glial cells	*Hmga2*, *Fgf13*, *Cit*, *Grin2b*, *Dner*
Neurogenesis	GO: 0001764; GO: 0048699; GO: 0022008; GO: 0010975; GO: 0120035; GO: 0031344	motor neurons	*Tafa1*, *Asic2*, *Dcc*, *Nrp1*, *Cntnap2*
Cell adhesion	GO: 0098742; GO: 0098609; GO: 0007155	motor neurons	*Dcc*, *Nrp1*, *Cntnap2*, *Ctnnd2*, *Il1rapl1*

GO analysis performed using PANTHER (PANTHER GO biological process complete; *$p < 0.05$, Fischer's exact test with Bonferroni correction for multiple testing).

astrocytic downregulation of interferon-stimulated genes in the spinal cord of these mice, which was suggested to be the result of decreased cGAS/STING pathway activity. In agreement, we observed a reduced expression of STING in GFAP-positive cells. Moreover, the link between *EGLN2* downregulation and the astrocytic interferon response was confirmed in patient-derived astrocytes. Hence, our study highlights the potential of EGLN2 as an ALS target mitigating motor neuron degeneration and normalizing the astrocytic pro-inflammatory interferon response *in vivo* and in patient-derived astrocytes.

ALS is characterized by motor neuron death, and patient-derived motor neurons recapitulate several disease phenotypes.[66] On the other hand, non-cell-autonomous mechanisms also contribute to ALS pathology.[67–69] Single-cell technology provides the opportunity to study the contribution of both motor neuron-intrinsic and -extrinsic pathways to the disease. As a result, several studies used this technology to investigate the transcriptional changes that mark the disease at a single-cell level.[70–73] In SOD1^{G93A} mice, snRNA-seq of the spinal cord identified that motor neurons and astrocytes underwent the most pronounced transcriptional changes at P90, including changes linked to increased ROS production in motor neurons and an increased inflammatory response in astrocytes.[71] Moreover, in postmortem motor and frontal cortices of C9orf72 ALS patients, excitatory neurons and astrocytes showed the largest transcriptomic alterations.[73] While single-cell RNA-seq is valuable to unravel the cell-specific transcriptomic signature of the disease, it can also be used to investigate potential therapeutic strategies to identify their underlying transcriptomic alterations at single-cell resolution. We applied this approach to investigate the cell-specific pathways that underlie EGLN2-mediated motor neuron protection in ALS.

The canonical target of EGLN2 is HIFα, affecting a range of pathways including rewired cellular metabolism.[8] Indeed, *Egln2* deletion did decrease the expression of genes linked to oxidative metabolism in neurons. However, the observed decreased expression of oxidative metabolism genes was suggested to be independent of HIF activation, as we did not observe any changes in the expression of HIF target genes in mice or zebrafish. A number of HIF- and hydroxylation-independent EGLN2 targets have been described and can give rise to a large variety of cell- and context-specific effects of EGLN2.[5] This was demonstrated by the HIF-independent protection of cortical neurons in stroke models.[11] In addition, we did not observe a downregulation of nuclear genes involved in the energy metabolism of motor neurons. This finding suggests that *Egln2*$^{-/-}$-induced motor neuron protection is not driven through metabolic rewiring.

snRNA-seq revealed that the loss of EGLN2 in the SOD1^{G93A} spinal cord induced an astrocyte-specific downregulation of pro-inflammatory interferon-stimulated genes. We considered this to be of particular interest because interferon-stimulated genes have been found to be upregulated in SOD1^{G93A} mice spinal cord astrocytes[74] and neuronal and myeloid cells from C9orf72[55,75,76] and TDP-43[77] patients with ALS and ALS models. Moreover, the latter showed that this increased interferon response was induced via cytoplasmic dsDNA-mediated cGAS/STING activation.[55,75–77] Our study provides insight into how astrocytes contribute to the increased cGAS/STING-induced interferon signaling in ALS,[55,74–79] underlining the contribution of non-cell-autonomous mechanisms,[67–69] and demonstrates that targeting EGLN2 can restore this response. Moreover, the effect of the loss of EGLN2 on the levels of interferon-stimulated genes in astrocytes was strengthened by the finding that knocking out *EGLN2* in patient iPSC-derived astrocytes normalized the levels of interferon-stimulated genes compared to *SOD1^{A4V}* astrocytes. In these *SOD1^{A4V}* patient-derived astrocytes, we observed a downregulation of interferon-stimulated genes and found that loss of EGLN2 increased these levels, contrary to our findings in SOD1^{G93A} mouse astrocytes. The difference in the levels of interferon-stimulated genes could be explained by the cell type, the stage of the disease, the involvement of other cell types, or the difference in the mutation. Astrocytes have been reported numerous times to play a unique role in ALS and neurodegeneration.[80] The reactive astrogliosis that occurs during neurodegeneration is not one fixed state but rather a dynamic process of multiple cellular states that can evolve over the disease course.[54] In agreement, RNA-seq analysis of SOD1^{G93A} versus WT astrocyte monocultures from P5 mice did not show differences in the transcriptomic interferon response,[81] while this was described to be present in astrocytes from P60 and P90 SOD1^{G93A} mice.[74] P110 in SOD1^{G93A} mice, most likely, models a later disease stage compared to the patient iPSC-derived astrocytes. As a result, different disease states and the presence of different stimuli due to the presence or absence of other cell types can explain the differences in interferon responses. While we did mimic neuroinflammation

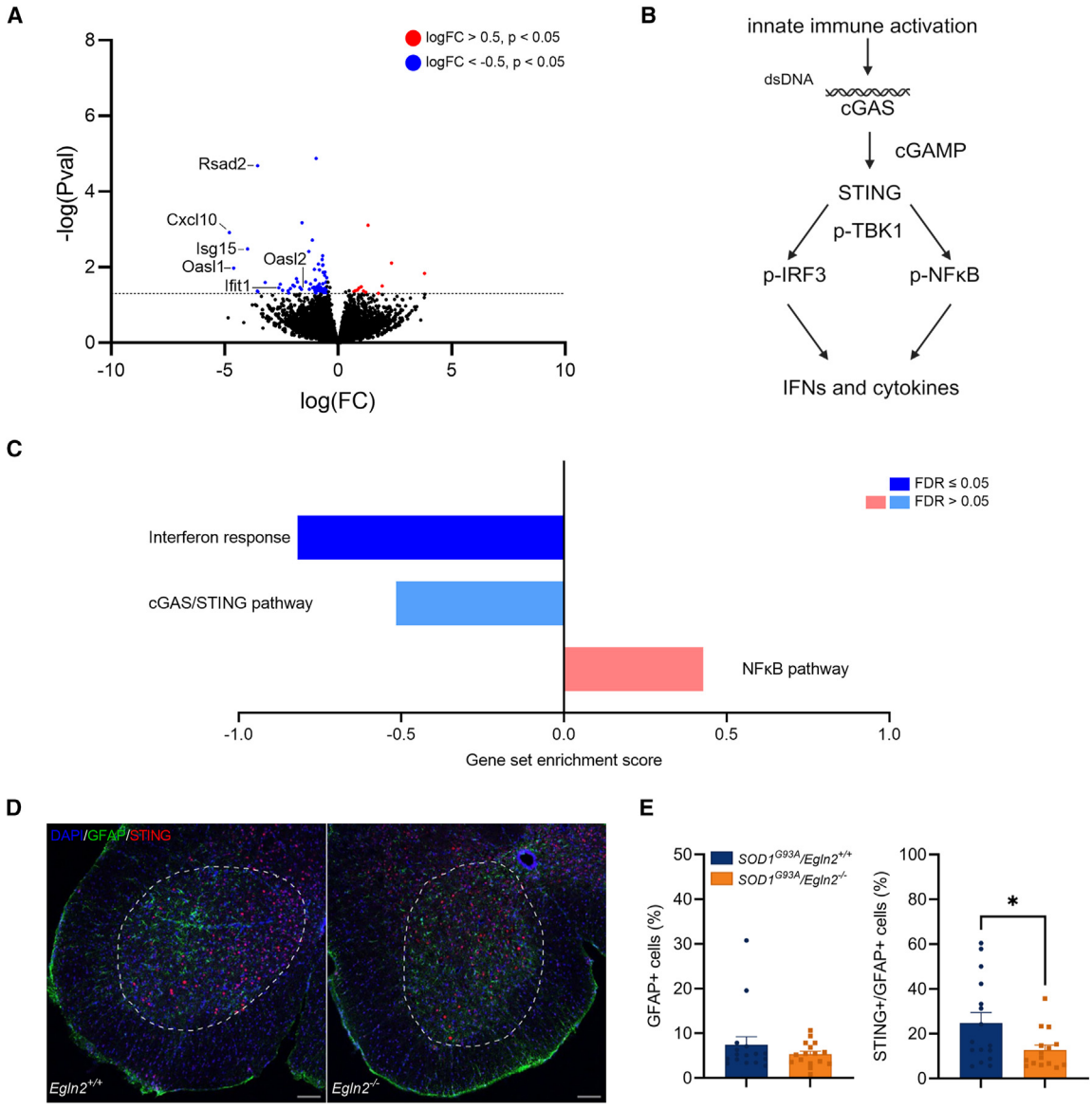

Figure 4. *Egln2* deletion induces astrocyte-specific downregulation of interferon-stimulated genes

(A) Volcano plot showing all DEGs in astrocytes from $SOD1^{G93A}/Egln2^{-/-}$ versus $SOD1^{G93A}/Egln2^{+/+}$ lumbar spinal cord at P110. Red indicates significant genes with upregulated expression (log10 (fold change) [log(FC)] > 0.5) in $SOD1^{G93A}/Egln2^{-/-}$ versus $SOD1^{G93A}/Egln2^{+/+}$ mice, and blue indicates significant genes with downregulated expression (log(FC) < −0.5) in $SOD1^{G93A}/Egln2^{-/-}$ versus $SOD1^{G93A}/Egln2^{+/+}$ mice.

(B) Graphical representation of the cGAS/STING and NF-κB pathways.

(C) Gene set enrichment analysis (GSEA) scores for interferon response,[55] cGAS/STING pathway,[56] and NF-κB pathway[55] in DEGs from $SOD1^{G93A}/Egln2^{-/-}$ versus $SOD1^{G93A}/Egln2^{+/+}$ astrocytes.

(D) Representative images of immunohistochemical analysis of 4′,6-diamidino-2-phenylindole (DAPI), glial fibrillary acidic protein (GFAP), and STING in the lumbar spinal cord ventral horn, indicated with a white dotted line, of $SOD1^{G93A}/Egln2^{+/+}$ and $SOD1^{G93A}/Egln2^{-/-}$ mice at P110. Scale bar, 50 μm.

(E) Quantification of number of GFAP-positive (GFAP+) cells and STING- and GFAP-positive (STING+/GFAP+) cells.

Data represent mean ± SEM, with the individual values of each lumbar spinal cord section shown ($N \geq 4$ mice per group). Statistical analyses were performed by an unpaired t test (*$p < 0.05$).

in vitro by treatment with a pro-inflammatory TIC cocktail that provokes astrocyte reactivity,[60] this still differs from the prolonged presence of a pro-inflammatory environment in the spinal cord of $SOD1^{G93A}$ mice. Finally, we must also consider that different (*SOD1*) mutations, while all resulting in ALS, could give rise to pathological differences.[82] Nevertheless, independent from the increased interferon response in $SOD1^{G93A}$ mice, as reported by Wang et al.,[74] or the decreased interferon response in $SOD1^{A4V}$ patient astrocytes that we observed, the deletion of *EGLN2* was able to normalize these levels.

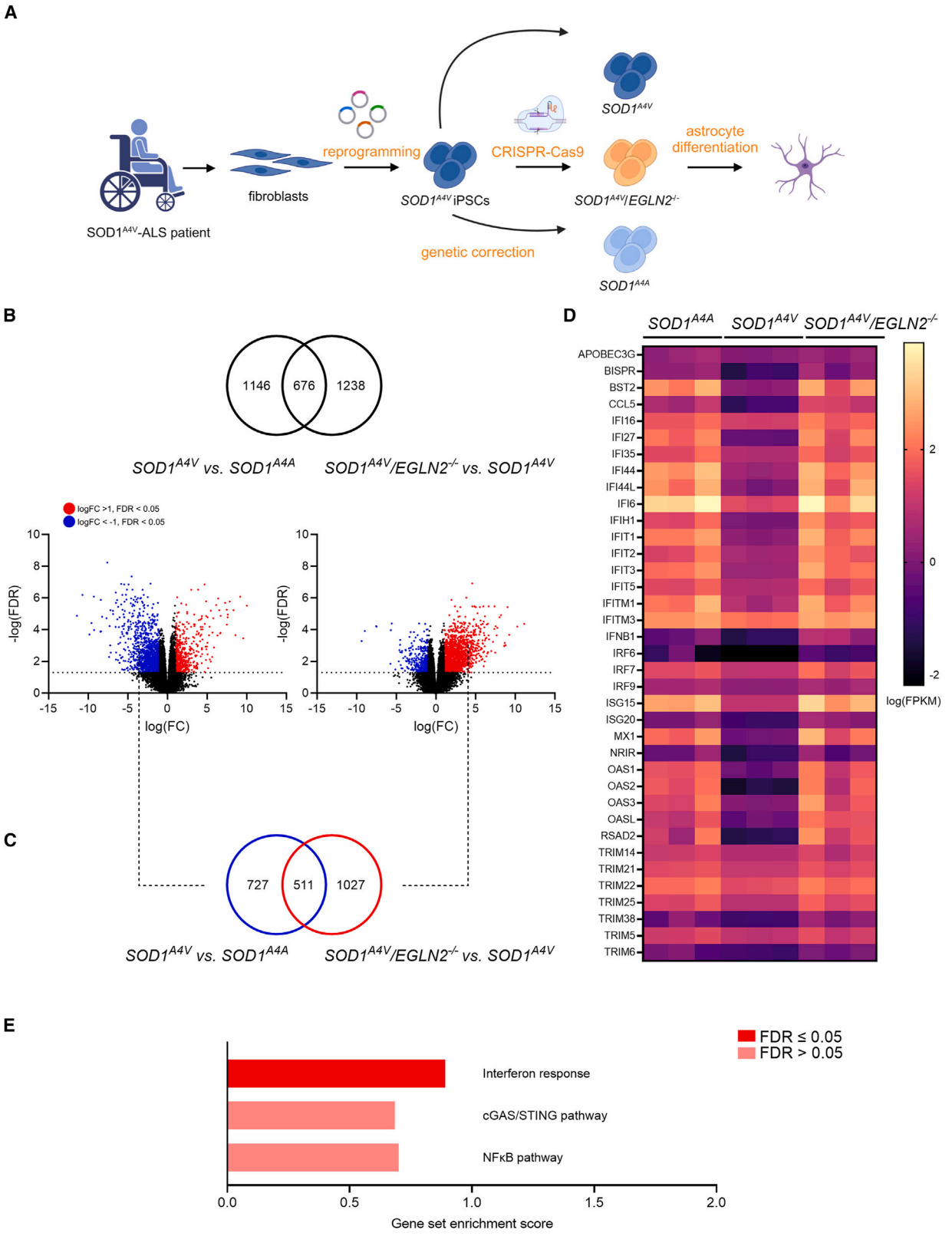

(legend on next page)

The ability of EGLN2 as target to provoke different disease-stage-dependent effects could be attributed to its sensor function enabling the enzyme to perceive the cellular state via the presence of oxygen, Fe^{2+}, ascorbic acid, or other metabolic intermediates.[2–4] The EGLN enzymes have been shown to act on the activator of the NF-κB pathway and the inducer of the inflammatory response, IKKβ.[12,83–85] GSEA on both *SOD1^{G93A}/Egln2$^{-/-}$* mouse astrocytes and *SOD1^{A4V}/EGLN2$^{-/-}$* iPSC-derived astrocytes showed an enrichment of the NF-κB pathway in the upregulated gene set, even when the interferon response was downregulated in *SOD1^{G93A}/Egln2$^{-/-}$* astrocytes. However, the transcriptomic effect of loss of EGLN2 on the cGAS/STING pathway was in line with the downstream effect on the interferon response, namely enrichment in the downregulated genes in *SOD1^{G93A}/Egln2$^{-/-}$* mouse astrocytes and the upregulated genes in *SOD1^{A4V}/EGLN2$^{-/-}$* human astrocytes. As a result, it seems likely that EGLN2 acts on the cGAS/STING pathway. In agreement with this, we observed a downregulation of STING protein expression in GFAP-positive cells in the spinal cord of *SOD1^{G93A}/Egln2$^{-/-}$* mice. Together, these results revealed that EGLN2 can directly or indirectly, for example via a decrease in ROS-induced mitochondrial DNA release,[9,77] modulate cGAS/STING pathway activity. As a result, our findings propose EGLN2 as a target that normalizes the cGAS/STING-induced interferon-driven neuroinflammatory response that characterizes motor neuron degeneration in ALS. This is supported by our observation that the neuroinflammation marker *Tspo*[52] was downregulated in *SOD1^{G93A}/Egln2$^{-/-}$* motor neurons.

In conclusion, our study demonstrates how targeting EGLN2 mitigates motor neuron degeneration in three different *in vivo* ALS models. Moreover, a link between EGLN2 and the astrocytic STING-induced interferon response was established using cell-specific tools such as snRNA-seq and patient-derived astrocytes. As a result, our data highlight EGLN2 as target that protects motor neurons and restores the interferon signaling pathway in astrocytes.

Limitations of the study

This study indicates that targeting EGLN2 might have therapeutic potential in different forms of ALS. However, the therapeutic potential should be further confirmed using additional approaches, such as ASO knockdown *in vivo*. Moreover, an ALS mouse model with an astrocyte-specific *Egln2* knockout would provide insight into what extent the motor neuron protection *in vivo* is driven by astrocytes. However, this would require the combination of three transgenic lines (homozygous floxed *Egln2*, astrocyte-specific Cre expression, and *SOD1^{G93A}* overexpression), with the extra complications that female *SOD1^{G93A}* mice are sterile, the birth rate of transgenic mice is approximately half of what can be expected, and the use of littermate controls is crucial given that a reduction of *hSOD1^{G93A}* copy number also affects survival.[86] Therefore, we used iPSC-derived astrocytes to confirm the direct effect of *EGLN2* deletion on astrocyte monocultures, with the additional advantage that these cells are human and patient derived. While these experiments, using one patient-isogenic control iPSC pair, confirmed that EGLN2 acts on the STING-induced interferon response in patient astrocytes, the confirmation of these findings in other familial and sporadic cell lines and other cell types, such as motor neurons, in mono- and/or co-culture would be a valuable addition to this study.

RESOURCE AVAILABILITY

Lead contact

Requests for further information, resources, and reagents should be directed to the lead contact, Ludo Van Den Bosch (ludo.vandenbosch@kuleuven.be).

Materials availability

Resources are available from the lead contact upon request.

Data and code availability

- The murine snRNA-seq data (GEO: GSE219201) and bulk iPSC-astrocyte RNA-seq data (GEO: GSE260913) are available on gene expression omnibus (GEO) via the aforementioned accession numbers.
- This paper does not report original code.
- Any additional information required to reanalyze the data reported in this work paper is available from the lead contact upon request.

ACKNOWLEDGMENTS

We gratefully thank the VIB Nucleomics Core for the library preparation and sequencing of the snRNA-seq and bulk RNA-seq experiment and statistical data analysis of the bulk RNA-seq experiment (https://nucleomicscore.sites.vib.be/en) and Dr. Antina de Boer for her help with the RNAscope experiment. This work was supported by VIB, the KU Leuven (C1; C14/17/107, C14/22/132, and "Opening the Future" Fund), the "Fund for Scientific Research Flanders" (FWO), ALS Liga Belgium ("A Cure for ALS"), and the Agency for Innovation by Science and Technology (150031). C.G. is supported by a fundamental PhD research grant awarded by the FWO (1174523N). T.V. has been supported by a strategic basic PhD research grant awarded by the FWO (1S60116N). P.C. is supported by grants from Methusalem funding (Flemish government), the Fund for Scientific Research-Flanders (FWO-Vlaanderen), and the European Research Council ERC Advanced Research Grants (EU-ERC743074 and EU-ERC101055155). P.V.D. holds a clinical investigatorship of the FWO and is supported by the E. von Behring Chair for Neuromuscular and Neurodegenerative Disorders, the fund "Een Hart voor ALS," and the "Laevers Fund for ALS Research." K.D.B. is endowed by the Wilhelm Schulthess

Figure 5. *EGLN2* deletion restores the level of interferon-stimulated genes in *SOD1^{A4V}* patient-derived astrocytes

(A) Schematic representation of the experimental setup.

(B) Venn diagram demonstrating the overlap between all significant DEGs in *SOD1^{A4V}* versus *SOD1^{A4A}* astrocytes (left volcano plot) and all significant DEGs in *SOD1^{A4V}/EGLN2$^{-/-}$* versus *SOD1^{A4V}* astrocytes (right volcano plot). Red indicates significant upregulated genes (log(FC) > 1), and blue indicates significant downregulated genes (log(FC) < −1).

(C) Venn diagram showing the overlap between the significantly downregulated genes in *SOD1^{A4V}* versus *SOD1^{A4A}* astrocytes (log(FC) < −1) and significantly upregulated genes in *SOD1^{A4V}/EGLN2$^{-/-}$* versus *SOD1^{A4V}* astrocytes (log(FC) > 1).

(D) Heatmap showing the expression levels (fragments per kilobase million [FPKM]) of interferon-stimulated genes in *SOD1^{A4A}*, *SOD1^{A4V}*, and *SOD1^{A4V}/EGLN2$^{-/-}$* astrocytes.

(E) GSEA scores for interferon response,[55] cGAS/STING pathway,[56] and NF-κB pathway[55] in DEGs from in *SOD1^{A4V}/EGLN2$^{-/-}$* versus *SOD1^{A4V}* astrocytes. *N* = 3 astrocyte differentiations.

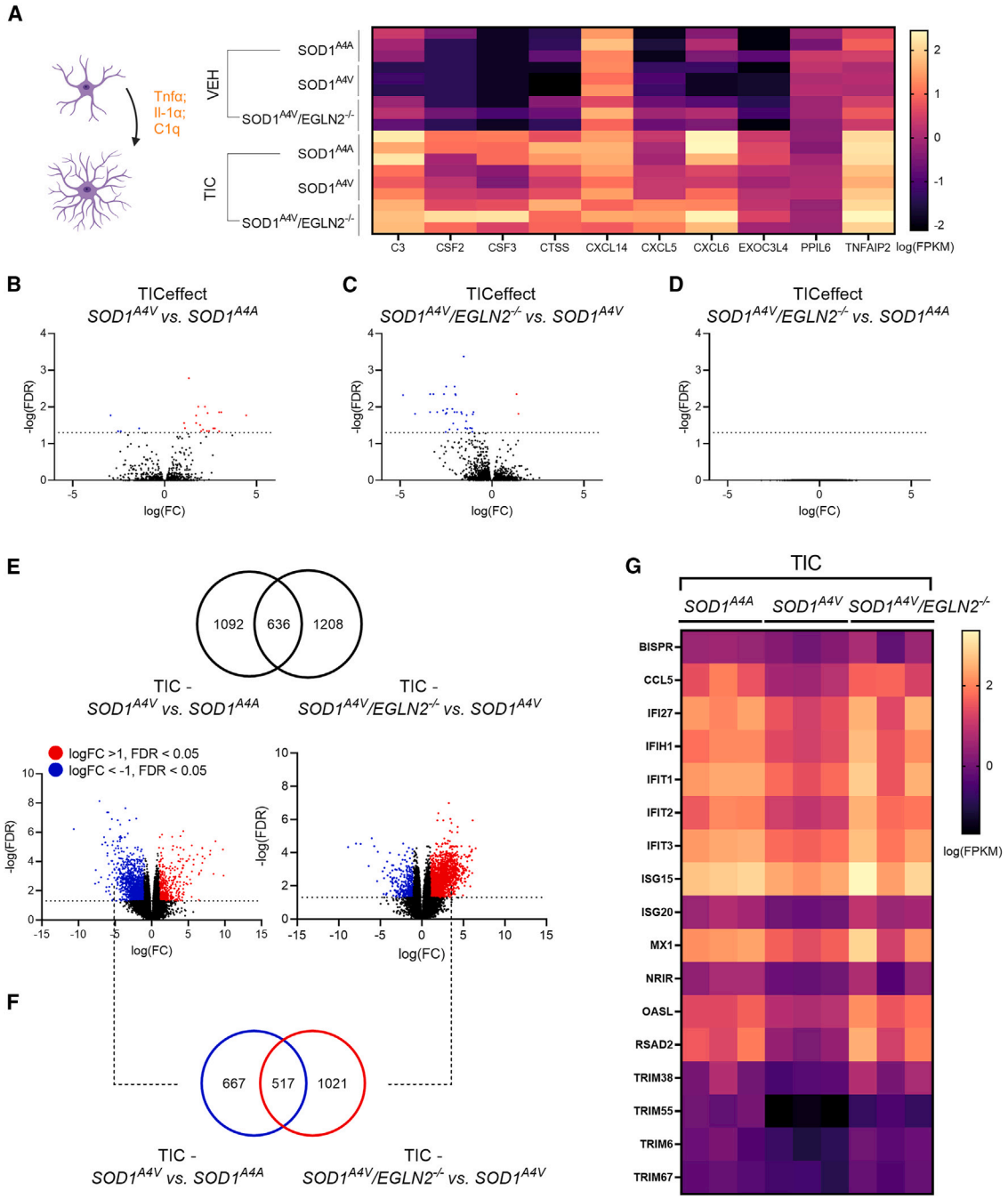

Figure 6. *EGLN2* deletion restores the levels of interferon-stimulated genes in reactive *SOD1*^{A4V} patient-derived astrocytes

(A) Heatmap showing the expression levels (FPKM) of reactive astrocyte marker genes in *SOD1*^{A4A}, *SOD1*^{A4V}, and *SOD1*^{A4V}/*EGLN2*$^{-/-}$ astrocytes treated with vehicle (VEH) or TNF-α, IL-1α, and C1q (TIC).

(B–D) Volcano plot showing all genes that respond differently to the TIC treatment in (B) *SOD1*^{A4V} versus *SOD1*^{A4A} astrocytes, (C) *SOD1*^{A4V}/*EGLN2*$^{-/-}$ versus *SOD1*^{A4V} astrocytes, and (D) *SOD1*^{A4V}/*EGLN2*$^{-/-}$ versus *SOD1*^{A4A} astrocytes. Red indicates significant upregulated genes (log(FC) > 1), and blue indicates significant downregulated genes (log(FC) < −1).

(E) Venn diagram showing the overlap between all significant DEGs in *SOD1*^{A4V} versus *SOD1*^{A4A} TIC-treated astrocytes (left volcano plot) and all significant DEGs in *SOD1*^{A4V}/*EGLN2*$^{-/-}$ versus *SOD1*^{A4V} TIC-treated astrocytes (right volcano plot).

(F) Venn diagram showing the overlap between the significantly downregulated genes in *SOD1*^{A4V} versus *SOD1*^{A4A} TIC-treated astrocytes (log(FC) < −1) and significantly upregulated genes in *SOD1*^{A4V}/*EGLN2*$^{-/-}$ versus *SOD1*^{A4V} TIC-treated astrocytes (log(FC) > 1).

(G) Heatmap showing the expression levels (FPKM) of interferon-stimulated genes in *SOD1*^{A4A}, *SOD1*^{A4V}, and *SOD1*^{A4V}/*EGLN2*$^{-/-}$ TIC-treated astrocytes. *N* = 3 astrocyte differentiations.

Foundation. L.V.D.B. is supported by the Generet Award for Rare Diseases. Figures 1A, 5A, and 6A were created with BioRender.com.

AUTHOR CONTRIBUTIONS

Conceptualization, C.G., T.V., A.Q., K.D.B., and L.V.D.B.; data curation, C.G., T.V., K.D., and M.M.; formal analysis, C.G., T.V., K.D., and M.M.; investigation, C.G., T.V., K.H., W.V., A. Sicart, C.E., L.D.C., F.N., and A.Q.; methodology, C.G., T.V., S.P., A. Sierksma, L.R., and F.N.; project administration, C.G. and T.V.; visualization, C.G. and T.V.; writing – original draft, C.G.; writing – review & editing, C.G., T.V., K.D., M.M., S.P., A. Sierksma, L.R., K.H., W.V., A. Sicart, C.E., L.D.C., F.N., A.Q., B.D.S., P.C., P.V.D., K.D.B., and L.V.D.B.; supervision, T.V., P.V.D., K.D.B., and L.V.D.B.; resources, B.D.S. and P.C.; funding acquisition, P.V.D. and L.V.D.B.

DECLARATION OF INTERESTS

T.V. is an employee of Bristol-Myers Squibb (Princeton, USA). B.D.S. has been a consultant for Eli Lilly and Company (Indianapolis, USA), Biogen (Cambridge, USA), Janssen Pharmaceutica (Beerse, Belgium), AbbVie, Inc. (North Chicago, USA), and others and is now a consultant for Eisai (Nutley, USA), Remynd (Leuven, Belgium), and Muna Therapeutics (Copenhagen, Denmark). B.D.S. is a scientific founder and stockholder of Muna Therapeutics. P.V.D. has served on advisory boards for Biogen, CSL Behring (King of Prussia, USA), Alexion Pharmaceuticals (Boston, USA), Ferrer (Barcelona, Spain), QurAlis (Cambridge, UK), Cytokinetics (South San Francisco, USA), Argenx (Boston, USA), UCB (Brussels, Belgium), Muna Therapeutics, Alector (South San Francisco, USA), Augustine Therapeutics (Leuven, Belgium), VectorY (Amsterdam, the Netherlands), Zambon (Bresso, Italy), and Amylyx (Cambridge, UK) (paid to institution). P.V.D. has received speaker fees from Biogen and Amylyx (paid to institution). P.V.D. has participated as an investigator in clinical trials on ALS sponsored by Biogen, Cytokinetics, Ferrer, Amylyx, Wave Life Sciences (Cambridge, UK), Corcept Therapeutics (Menlo Park, USA), Transposon Therapeutics (Westport, USA), Sanofi (Paris, France), AB Science (Paris, France), IONIS Pharmaceuticals (Carlsbad, USA), Apellis Pharmaceuticals (Waltham, USA), Alexion Pharmaceuticals, Orphazyme (Copenhagen, Denmark), Orion Pharma (Espoo, Finland), and AL-S Pharma (Schlieren, Switzerland). P.V.D. is supported by the E. von Behring Chair for Neuromuscular and Neurodegenerative Disorders (from CSL Behring, paid to institution). L.V.D.B. is head of the scientific advisory board of Augustine Therapeutics and is part of the investment advisory board of Droia Ventures (Meise, Belgium). L.V.D.B. and B.D.S. are scientific founders of Augustine Therapeutics.

STAR★METHODS

Detailed methods are provided in the online version of this paper and include the following:

- KEY RESOURCES TABLE
- EXPERIMENTAL MODEL AND STUDY PARTICIPANT DETAILS
  - Zebrafish
  - Mice
  - iPSCs
- METHOD DETAILS
  - Zebrafish *DNA constructs and AMO*
  - Mice disease onset and survival
  - Mice motor neuron counts
  - Generation and quality control of EGLN2 knock-out iPSCs
  - Generation of iPSC-derived astrocytes
  - Immunofluorescence
  - RNA isolation, qRT-PCR and RT-PCR
  - Western blot analysis
  - Single-nuclei RNA sequencing of mice lumbar spinal cord
  - RNAScope *in situ* hybridization
  - RNA sequencing of iPSC-derived astrocytes
- QUANTIFICATION AND STATISTICAL ANALYSIS

SUPPLEMENTAL INFORMATION

Supplemental information can be found online at https://doi.org/10.1016/j.celrep.2024.114719.

Received: March 7, 2024
Revised: July 8, 2024
Accepted: August 20, 2024

REFERENCES

1. Semenza, G.L. (2011). Oxygen sensing, homeostasis, and disease. N. Engl. J. Med. *365*, 537–547. https://doi.org/10.1056/NEJMra1011165.
2. Selak, M.A., Armour, S.M., MacKenzie, E.D., Boulahbel, H., Watson, D.G., Mansfield, K.D., Pan, Y., Simon, M.C., Thompson, C.B., and Gottlieb, E. (2005). Succinate links TCA cycle dysfunction to oncogenesis by inhibiting HIF-alpha prolyl hydroxylase. Cancer Cell *7*, 77–85. https://doi.org/10.1016/j.ccr.2004.11.022.
3. Isaacs, J.S., Jung, Y.J., Mole, D.R., Lee, S., Torres-Cabala, C., Chung, Y.L., Merino, M., Trepel, J., Zbar, B., Toro, J., et al. (2005). HIF overexpression correlates with biallelic loss of fumarate hydratase in renal cancer: novel role of fumarate in regulation of HIF stability. Cancer Cell *8*, 143–153. https://doi.org/10.1016/j.ccr.2005.06.017.
4. Schofield, C.J., and Ratcliffe, P.J. (2004). Oxygen sensing by HIF hydroxylases. Nat. Rev. Mol. Cell Biol. *5*, 343–354. https://doi.org/10.1038/nrm1366.
5. Wong, B.W., Kuchnio, A., Bruning, U., and Carmeliet, P. (2013). Emerging novel functions of the oxygen-sensing prolyl hydroxylase domain enzymes. Trends Biochem. Sci. *38*, 3–11. https://doi.org/10.1016/j.tibs.2012.10.004.
6. Epstein, A.C., Gleadle, J.M., McNeill, L.A., Hewitson, K.S., O'Rourke, J., Mole, D.R., Mukherji, M., Metzen, E., Wilson, M.I., Dhanda, A., et al. (2001). C. elegans EGL-9 and mammalian homologs define a family of dioxygenases that regulate HIF by prolyl hydroxylation. Cell *107*, 43–54. https://doi.org/10.1016/s0092-8674(01)00507-4.
7. Bruick, R.K., and McKnight, S.L. (2001). A conserved family of prolyl-4-hydroxylases that modify HIF. Science *294*, 1337–1340. https://doi.org/10.1126/science.1066373.
8. Ivan, M., and Kaelin, W.G. (2017). The EGLN-HIF O_2-Sensing System: Multiple Inputs and Feedbacks. Mol. Cell *66*, 772–779. https://doi.org/10.1016/j.molcel.2017.06.002.
9. Aragonés, J., Schneider, M., Van Geyte, K., Fraisl, P., Dresselaers, T., Mazzone, M., Dirkx, R., Zacchigna, S., Lemieux, H., Jeoung, N.H., et al. (2008). Deficiency or inhibition of oxygen sensor Phd1 induces hypoxia tolerance by reprogramming basal metabolism. Nat. Genet. *40*, 170–180. https://doi.org/10.1038/ng.2007.62.
10. Schneider, M., Van Geyte, K., Fraisl, P., Kiss, J., Aragonés, J., Mazzone, M., Mairbäurl, H., De Bock, K., Jeoung, N.H., Mollenhauer, M., et al. (2010). Loss or silencing of the PHD1 prolyl hydroxylase protects livers of mice against ischemia/reperfusion injury. Gastroenterology *138*, 1143–1154.e542. https://doi.org/10.1053/j.gastro.2009.09.057.
11. Quaegebeur, A., Segura, I., Schmieder, R., Verdegem, D., Decimo, I., Bifari, F., Dresselaers, T., Eelen, G., Ghosh, D., Davidson, S.M., et al. (2016). Deletion or Inhibition of the Oxygen Sensor PHD1 Protects against Ischemic Stroke via Reprogramming of Neuronal Metabolism. Cell Metabol. *23*, 280–291. https://doi.org/10.1016/j.cmet.2015.12.007.
12. Cummins, E.P., Berra, E., Comerford, K.M., Ginouves, A., Fitzgerald, K.T., Seeballuck, F., Godson, C., Nielsen, J.E., Moynagh, P., Pouyssegur, J., and Taylor, C.T. (2006). Prolyl hydroxylase-1 negatively regulates IkappaB kinase-beta, giving insight into hypoxia-induced NFkappaB activity. Proc. Natl. Acad. Sci. USA *103*, 18154–18159. https://doi.org/10.1073/pnas.0602235103.

13. Van Welden, S., De Vos, M., Wielockx, B., Tavernier, S.J., Dullaers, M., Neyt, S., Descamps, B., Devisscher, L., Devriese, S., Van den Bossche, L., et al. (2017). Haematopoietic prolyl hydroxylase-1 deficiency promotes M2 macrophage polarization and is both necessary and sufficient to protect against experimental colitis. J. Pathol. *241*, 547–558. https://doi.org/10.1002/path.4861.

14. Wilson, D.M., Cookson, M.R., Van Den Bosch, L., Zetterberg, H., Holtzman, D.M., and Dewachter, I. (2023). Hallmarks of neurodegenerative diseases. Cell *186*, 693–714. https://doi.org/10.1016/j.cell.2022.12.032.

15. Shaw, P.J., Ince, P.G., Falkous, G., and Mantle, D. (1995). Oxidative damage to protein in sporadic motor neuron disease spinal cord. Ann. Neurol. *38*, 691–695. https://doi.org/10.1002/ana.410380424.

16. Ferrante, R.J., Browne, S.E., Shinobu, L.A., Bowling, A.C., Baik, M.J., MacGarvey, U., Kowall, N.W., Brown, R.H., Jr., and Beal, M.F. (1997). Evidence of increased oxidative damage in both sporadic and familial amyotrophic lateral sclerosis. J. Neurochem. *69*, 2064–2074.

17. Patel, M. (2016). Targeting Oxidative Stress in Central Nervous System Disorders. Trends Pharmacol. Sci. *37*, 768–778. https://doi.org/10.1016/j.tips.2016.06.007.

18. Vandoorne, T., De Bock, K., and Van Den Bosch, L. (2018). Energy metabolism in ALS: an underappreciated opportunity? Acta Neuropathol. *135*, 489–509. https://doi.org/10.1007/s00401-018-1835-x.

19. Germeys, C., Vandoorne, T., Bercier, V., and Van Den Bosch, L. (2019). Existing and Emerging Metabolomic Tools for ALS Research. Genes *10*, 1011. https://doi.org/10.3390/genes10121011.

20. Kupershmidt, L., Weinreb, O., Amit, T., Mandel, S., Carri, M.T., and Youdim, M.B.H. (2009). Neuroprotective and neuritogenic activities of novel multimodal iron-chelating drugs in motor-neuron-like NSC-34 cells and transgenic mouse model of amyotrophic lateral sclerosis. Faseb. J. *23*, 3766–3779. https://doi.org/10.1096/fj.09-130047.

21. Nomura, E., Ohta, Y., Tadokoro, K., Shang, J., Feng, T., Liu, X., Shi, X., Matsumoto, N., Sasaki, R., Tsunoda, K., et al. (2019). Imaging Hypoxic Stress and the Treatment of Amyotrophic Lateral Sclerosis with Dimethyloxalylglycine in a Mice Model. Neuroscience *415*, 31–43. https://doi.org/10.1016/j.neuroscience.2019.06.025.

22. Oosthuyse, B., Moons, L., Storkebaum, E., Beck, H., Nuyens, D., Brusselmans, K., Van Dorpe, J., Hellings, P., Gorselink, M., Heymans, S., et al. (2001). Deletion of the hypoxia-response element in the vascular endothelial growth factor promoter causes motor neuron degeneration. Nat. Genet. *28*, 131–138. https://doi.org/10.1038/88842.

23. Storkebaum, E., Lambrechts, D., Dewerchin, M., Moreno-Murciano, M.P., Appelmans, S., Oh, H., Van Damme, P., Rutten, B., Man, W.Y., De Mol, M., et al. (2005). Treatment of motoneuron degeneration by intracerebroventricular delivery of VEGF in a rat model of ALS. Nat. Neurosci. *8*, 85–92. https://doi.org/10.1038/nn1360.

24. Van Den Bosch, L., Storkebaum, E., Vleminckx, V., Moons, L., Vanopdenbosch, L., Scheveneels, W., Carmeliet, P., and Robberecht, W. (2004). Effects of vascular endothelial growth factor (VEGF) on motor neuron degeneration. Neurobiol. Dis. *17*, 21–28. https://doi.org/10.1016/j.nbd.2004.06.004.

25. Liu, J., and Wang, F. (2017). Role of Neuroinflammation in Amyotrophic Lateral Sclerosis: Cellular Mechanisms and Therapeutic Implications. Front. Immunol. *8*, 1005. https://doi.org/10.3389/fimmu.2017.01005.

26. Henkel, J.S., Beers, D.R., Siklós, L., and Appel, S.H. (2006). The chemokine MCP-1 and the dendritic and myeloid cells it attracts are increased in the mSOD1 mouse model of ALS. Mol. Cell. Neurosci. *31*, 427–437. https://doi.org/10.1016/j.mcn.2005.10.016.

27. Mishra, P.S., Dhull, D.K., Nalini, A., Vijayalakshmi, K., Sathyaprabha, T.N., Alladi, P.A., and Raju, T.R. (2016). Astroglia acquires a toxic neuroinflammatory role in response to the cerebrospinal fluid from amyotrophic lateral sclerosis patients. J. Neuroinflammation *13*, 212. https://doi.org/10.1186/s12974-016-0698-0.

28. Kuhle, J., Lindberg, R.L.P., Regeniter, A., Mehling, M., Steck, A.J., Kappos, L., and Czaplinski, A. (2009). Increased levels of inflammatory chemokines in amyotrophic lateral sclerosis. Eur. J. Neurol. *16*, 771–774. https://doi.org/10.1111/j.1468-1331.2009.02560.x.

29. Jin, M., Günther, R., Akgün, K., Hermann, A., and Ziemssen, T. (2020). Peripheral proinflammatory Th1/Th17 immune cell shift is linked to disease severity in amyotrophic lateral sclerosis. Sci. Rep. *10*, 5941. https://doi.org/10.1038/s41598-020-62756-8.

30. Frakes, A.E., Ferraiuolo, L., Haidet-Phillips, A.M., Schmelzer, L., Braun, L., Miranda, C.J., Ladner, K.J., Bevan, A.K., Foust, K.D., Godbout, J.P., et al. (2014). Microglia induce motor neuron death via the classical NF-κB pathway in amyotrophic lateral sclerosis. Neuron *81*, 1009–1023. https://doi.org/10.1016/j.neuron.2014.01.013.

31. Crosio, C., Valle, C., Casciati, A., Iaccarino, C., and Carrì, M.T. (2011). Astroglial inhibition of NF-κB does not ameliorate disease onset and progression in a mouse model for amyotrophic lateral sclerosis (ALS). PLoS One *6*, e17187. https://doi.org/10.1371/journal.pone.0017187.

32. Lemmens, R., Van Hoecke, A., Hersmus, N., Geelen, V., D'Hollander, I., Thijs, V., Van Den Bosch, L., Carmeliet, P., and Robberecht, W. (2007). Overexpression of mutant superoxide dismutase 1 causes a motor axonopathy in the zebrafish. Hum. Mol. Genet. *16*, 2359–2365. https://doi.org/10.1093/hmg/ddm193.

33. Aragones, J., Schneider, M., Van Geyte, K., Fraisl, P., Dresselaers, T., Mazzone, M., Dirkx, R., Zacchigna, S., Lemieux, H., Jeoung, N.H., et al. (2008). Deficiency or inhibition of oxygen sensor Phd1 induces hypoxia tolerance by reprogramming basal metabolism. Nat. Genet. *40*, 170–180. https://doi.org/10.1038/ng.2007.62.

34. Gurney, M.E., Pu, H., Chiu, A.Y., Dal Canto, M.C., Polchow, C.Y., Alexander, D.D., Caliendo, J., Hentati, A., Kwon, Y.W., and Deng, H.X. (1994). Motor neuron degeneration in mice that express a human Cu,Zn superoxide dismutase mutation. Science *264*, 1772–1775. https://doi.org/10.1126/science.8209258.

35. Sathyamurthy, A., Johnson, K.R., Matson, K.J.E., Dobrott, C.I., Li, L., Ryba, A.R., Bergman, T.B., Kelly, M.C., Kelley, M.W., and Levine, A.J. (2018). Massively Parallel Single Nucleus Transcriptional Profiling Defines Spinal Cord Neurons and Their Activity during Behavior. Cell Rep. *22*, 2216–2225. https://doi.org/10.1016/j.celrep.2018.02.003.

36. Rosenberg, A.B., Roco, C.M., Muscat, R.A., Kuchina, A., Sample, P., Yao, Z., Graybuck, L.T., Peeler, D.J., Mukherjee, S., Chen, W., et al. (2018). Single-cell profiling of the developing mouse brain and spinal cord with split-pool barcoding. Science *360*, 176–182. https://doi.org/10.1126/science.aam8999.

37. Delile, J., Rayon, T., Melchionda, M., Edwards, A., Briscoe, J., and Sagner, A. (2019). Single cell transcriptomics reveals spatial and temporal dynamics of gene expression in the developing mouse spinal cord. Development *146*, dev173807. https://doi.org/10.1242/dev.173807.

38. Zeisel, A., Hochgerner, H., Lönnerberg, P., Johnsson, A., Memic, F., van der Zwan, J., Häring, M., Braun, E., Borm, L.E., La Manno, G., et al. (2018). Molecular Architecture of the Mouse Nervous System. Cell *174*, 999–1014.e1022. https://doi.org/10.1016/j.cell.2018.06.021.

39. Artegiani, B., Lyubimova, A., Muraro, M., van Es, J.H., van Oudenaarden, A., and Clevers, H. (2017). A Single-Cell RNA Sequencing Study Reveals Cellular and Molecular Dynamics of the Hippocampal Neurogenic Niche. Cell Rep. *21*, 3271–3284. https://doi.org/10.1016/j.celrep.2017.11.050.

40. Zhang, Y., Chen, K., Sloan, S.A., Bennett, M.L., Scholze, A.R., O'Keeffe, S., Phatnani, H.P., Guarnieri, P., Caneda, C., Ruderisch, N., et al. (2014). An RNA-sequencing transcriptome and splicing database of glia, neurons, and vascular cells of the cerebral cortex. J. Neurosci. *34*, 11929–11947. https://doi.org/10.1523/JNEUROSCI.1860-14.2014.

41. Blum, J.A., Klemm, S., Shadrach, J.L., Guttenplan, K.A., Nakayama, L., Kathiria, A., Hoang, P.T., Gautier, O., Kaltschmidt, J.A., Greenleaf, W.J., and Gitler, A.D. (2021). Single-cell transcriptomic analysis of the adult mouse spinal cord reveals molecular diversity of autonomic and

skeletal motor neurons. Nat. Neurosci. *24*, 572–583. https://doi.org/10.1038/s41593-020-00795-0.

42. Alkaslasi, M.R., Piccus, Z.E., Hareendran, S., Silberberg, H., Chen, L., Zhang, Y., Petros, T.J., and Le Pichon, C.E. (2021). Single nucleus RNA-sequencing defines unexpected diversity of cholinergic neuron types in the adult mouse spinal cord. Nat. Commun. *12*, 2471. https://doi.org/10.1038/s41467-021-22691-2.
43. Russ, D.E., Cross, R.B.P., Li, L., Koch, S.C., Matson, K.J.E., Yadav, A., Alkaslasi, M.R., Lee, D.I., Le Pichon, C.E., Menon, V., and Levine, A.J. (2021). A harmonized atlas of mouse spinal cord cell types and their spatial organization. Nat. Commun. *12*, 5722. https://doi.org/10.1038/s41467-021-25125-1.
44. Melamed, Z., López-Erauskin, J., Baughn, M.W., Zhang, O., Drenner, K., Sun, Y., Freyermuth, F., McMahon, M.A., Beccari, M.S., Artates, J.W., et al. (2019). Premature polyadenylation-mediated loss of stathmin-2 is a hallmark of TDP-43-dependent neurodegeneration. Nat. Neurosci. *22*, 180–190. https://doi.org/10.1038/s41593-018-0293-z.
45. Klim, J.R., Williams, L.A., Limone, F., Guerra San Juan, I., Davis-Dusenbery, B.N., Mordes, D.A., Burberry, A., Steinbaugh, M.J., Gamage, K.K., Kirchner, R., et al. (2019). ALS-implicated protein TDP-43 sustains levels of STMN2, a mediator of motor neuron growth and repair. Nat. Neurosci. *22*, 167–179. https://doi.org/10.1038/s41593-018-0300-4.
46. Morello, G., Guarnaccia, M., Spampinato, A.G., La Cognata, V., D'Agata, V., and Cavallaro, S. (2018). Copy Number Variations in Amyotrophic Lateral Sclerosis: Piecing the Mosaic Tiles Together through a Systems Biology Approach. Mol. Neurobiol. *55*, 1299–1322. https://doi.org/10.1007/s12035-017-0393-x.
47. Lee, S., Jeon, Y.M., Cha, S.J., Kim, S., Kwon, Y., Jo, M., Jang, Y.N., Lee, S., Kim, J., Kim, S.R., et al. (2020). PTK2/FAK regulates UPS impairment via SQSTM1/p62 phosphorylation in TARDBP/TDP-43 proteinopathies. Autophagy *16*, 1396–1412. https://doi.org/10.1080/15548627.2019.1686729.
48. Mòdol-Caballero, G., García-Lareu, B., Verdés, S., Ariza, L., Sánchez-Brualla, I., Brocard, F., Bosch, A., Navarro, X., and Herrando-Grabulosa, M. (2020). Therapeutic Role of Neuregulin 1 Type III in SOD1-Linked Amyotrophic Lateral Sclerosis. Neurotherapeutics *17*, 1048–1060. https://doi.org/10.1007/s13311-019-00811-7.
49. Tollervey, J.R., Curk, T., Rogelj, B., Briese, M., Cereda, M., Kayikci, M., König, J., Hortobágyi, T., Nishimura, A.L., Zupunski, V., et al. (2011). Characterizing the RNA targets and position-dependent splicing regulation by TDP-43. Nat. Neurosci. *14*, 452–458. https://doi.org/10.1038/nn.2778.
50. Oeckl, P., Weydt, P., Thal, D.R., Weishaupt, J.H., Ludolph, A.C., and Otto, M. (2020). Proteomics in cerebrospinal fluid and spinal cord suggests UCHL1, MAP2 and GPNMB as biomarkers and underpins importance of transcriptional pathways in amyotrophic lateral sclerosis. Acta Neuropathol. *139*, 119–134. https://doi.org/10.1007/s00401-019-02093-x.
51. Lee, S., Shang, Y., Redmond, S.A., Urisman, A., Tang, A.A., Li, K.H., Burlingame, A.L., Pak, R.A., Jovičić, A., Gitler, A.D., et al. (2016). Activation of HIPK2 Promotes ER Stress-Mediated Neurodegeneration in Amyotrophic Lateral Sclerosis. Neuron *91*, 41–55. https://doi.org/10.1016/j.neuron.2016.05.021.
52. Lee, Y., Park, Y., Nam, H., Lee, J.W., and Yu, S.W. (2020). Translocator protein (TSPO): the new story of the old protein in neuroinflammation. BMB Rep. *53*, 20–27. https://doi.org/10.5483/BMBRep.2020.53.1.273.
53. Chew, S., and Atassi, N. (2019). Positron Emission Tomography Molecular Imaging Biomarkers for Amyotrophic Lateral Sclerosis. Front. Neurol. *10*, 135. https://doi.org/10.3389/fneur.2019.00135.
54. Escartin, C., Galea, E., Lakatos, A., O'Callaghan, J.P., Petzold, G.C., Serrano-Pozo, A., Steinhäuser, C., Volterra, A., Carmignoto, G., Agarwal, A., et al. (2021). Reactive astrocyte nomenclature, definitions, and future directions. Nat. Neurosci. *24*, 312–325. https://doi.org/10.1038/s41593-020-00783-4.
55. McCauley, M.E., O'Rourke, J.G., Yáñez, A., Markman, J.L., Ho, R., Wang, X., Chen, S., Lall, D., Jin, M., Muhammad, A.K.M.G., et al. (2020). C9orf72 in myeloid cells suppresses STING-induced inflammation. Nature *585*, 96–101. https://doi.org/10.1038/s41586-020-2625-x.
56. Paul, B.D., Snyder, S.H., and Bohr, V.A. (2021). Signaling by cGAS-STING in Neurodegeneration, Neuroinflammation, and Aging. Trends Neurosci. *44*, 83–96. https://doi.org/10.1016/j.tins.2020.10.008.
57. Kiskinis, E., Sandoe, J., Williams, L.A., Boulting, G.L., Moccia, R., Wainger, B.J., Han, S., Peng, T., Thams, S., Mikkilineni, S., et al. (2014). Pathways disrupted in human ALS motor neurons identified through genetic correction of mutant SOD1. Cell Stem Cell *14*, 781–795. https://doi.org/10.1016/j.stem.2014.03.004.
58. Yang, W.W., Sidman, R.L., Taksir, T.V., Treleaven, C.M., Fidler, J.A., Cheng, S.H., Dodge, J.C., and Shihabuddin, L.S. (2011). Relationship between neuropathology and disease progression in the SOD1(G93A) ALS mouse. Exp. Neurol. *227*, 287–295. https://doi.org/10.1016/j.expneurol.2010.11.019.
59. Barbar, L., Jain, T., Zimmer, M., Kruglikov, I., Sadick, J.S., Wang, M., Kalpana, K., Rose, I.V.L., Burstein, S.R., Rusielewicz, T., et al. (2020). CD49f Is a Novel Marker of Functional and Reactive Human iPSC-Derived Astrocytes. Neuron *107*, 436–453.e12. https://doi.org/10.1016/j.neuron.2020.05.014.
60. Liddelow, S.A., Guttenplan, K.A., Clarke, L.E., Bennett, F.C., Bohlen, C.J., Schirmer, L., Bennett, M.L., Münch, A.E., Chung, W.S., Peterson, T.C., et al. (2017). Neurotoxic reactive astrocytes are induced by activated microglia. Nature *541*, 481–487. https://doi.org/10.1038/nature21029.
61. Ziff, O.J., Clarke, B.E., Taha, D.M., Crerar, H., Luscombe, N.M., and Patani, R. (2022). Meta-analysis of human and mouse ALS astrocytes reveals multi-omic signatures of inflammatory reactive states. Genome Res. *32*, 71–84. https://doi.org/10.1101/gr.275939.121.
62. Tyzack, G.E., Hall, C.E., Sibley, C.R., Cymes, T., Forostyak, S., Carlino, G., Meyer, I.F., Schiavo, G., Zhang, S.C., Gibbons, G.M., et al. (2017). A neuroprotective astrocyte state is induced by neuronal signal EphB1 but fails in ALS models. Nat. Commun. *8*, 1164. https://doi.org/10.1038/s41467-017-01283-z.
63. Stoklund Dittlau, K., Terrie, L., Baatsen, P., Kerstens, A., De Swert, L., Janky, R., Corthout, N., Masrori, P., Van Damme, P., Hyttel, P., et al. (2023). FUS-ALS hiPSC-derived astrocytes impair human motor units through both gain-of-toxicity and loss-of-support mechanisms. Mol. Neurodegener. *18*, 5. https://doi.org/10.1186/s13024-022-00591-3.
64. Neyrinck, K., Van Den Daele, J., Vervliet, T., De Smedt, J., Wierda, K., Nijs, M., Vanbokhoven, T., D'hondt, A., Planque, M., Fendt, S.M., et al. (2021). SOX9-induced Generation of Functional Astrocytes Supporting Neuronal Maturation in an All-human System. Stem Cell Rev. Rep. *17*, 1855–1873. https://doi.org/10.1007/s12015-021-10179-x.
65. Birger, A., Ben-Dor, I., Ottolenghi, M., Turetsky, T., Gil, Y., Sweetat, S., Perez, L., Belzer, V., Casden, N., Steiner, D., et al. (2019). Human iPSC-derived astrocytes from ALS patients with mutated C9ORF72 show increased oxidative stress and neurotoxicity. EBioMedicine *50*, 274–289. https://doi.org/10.1016/j.ebiom.2019.11.026.
66. Guo, W., Fumagalli, L., Prior, R., and Van Den Bosch, L. (2017). Current Advances and Limitations in Modeling ALS/FTD in a Dish Using Induced Pluripotent Stem Cells. Front. Neurosci. *11*, 671. https://doi.org/10.3389/fnins.2017.00671.
67. Boillée, S., Vande Velde, C., and Cleveland, D.W. (2006). ALS: a disease of motor neurons and their nonneuronal neighbors. Neuron *52*, 39–59. https://doi.org/10.1016/j.neuron.2006.09.018.
68. Vahsen, B.F., Gray, E., Thompson, A.G., Ansorge, O., Anthony, D.C., Cowley, S.A., Talbot, K., and Turner, M.R. (2021). Non-neuronal cells in amyotrophic lateral sclerosis - from pathogenesis to biomarkers. Nat. Rev. Neurol. *17*, 333–348. https://doi.org/10.1038/s41582-021-00487-8.
69. Van Harten, A.C.M., Phatnani, H., and Przedborski, S. (2021). Non-cell-autonomous pathogenic mechanisms in amyotrophic lateral sclerosis.

Trends Neurosci. *44*, 658–668. https://doi.org/10.1016/j.tins.2021.04.008.

70. Liu, W., Venugopal, S., Majid, S., Ahn, I.S., Diamante, G., Hong, J., Yang, X., and Chandler, S.H. (2020). Single-cell RNA-seq analysis of the brainstem of mutant SOD1 mice reveals perturbed cell types and pathways of amyotrophic lateral sclerosis. Neurobiol. Dis. *141*, 104877. https://doi.org/10.1016/j.nbd.2020.104877.
71. MacLean, M., López-Díez, R., Vasquez, C., Gugger, P.F., and Schmidt, A.M. (2022). Neuronal-glial communication perturbations in murine SOD1. Commun. Biol. *5*, 177. https://doi.org/10.1038/s42003-022-03128-y.
72. Maniatis, S., Äijö, T., Vickovic, S., Braine, C., Kang, K., Mollbrink, A., Fagegaltier, D., Andrusivová, Ž., Saarenpää, S., Saiz-Castro, G., et al. (2019). Spatiotemporal dynamics of molecular pathology in amyotrophic lateral sclerosis. Science *364*, 89–93. https://doi.org/10.1126/science.aav9776.
73. Li, J., Jaiswal, M.K., Chien, J.F., Kozlenkov, A., Jung, J., Zhou, P., Gardashli, M., Pregent, L.J., Engelberg-Cook, E., Dickson, D.W., et al. (2023). Divergent single cell transcriptome and epigenome alterations in ALS and FTD patients with C9orf72 mutation. Nat. Commun. *14*, 5714. https://doi.org/10.1038/s41467-023-41033-y.
74. Wang, R., Yang, B., and Zhang, D. (2011). Activation of interferon signaling pathways in spinal cord astrocytes from an ALS mouse model. Glia *59*, 946–958. https://doi.org/10.1002/glia.21167.
75. Rodriguez, S., Sahin, A., Schrank, B.R., Al-Lawati, H., Costantino, I., Benz, E., Fard, D., Albers, A.D., Cao, L., Gomez, A.C., et al. (2021). Genome-encoded cytoplasmic double-stranded RNAs, found in C9ORF72 ALS-FTD brain, propagate neuronal loss. Sci. Transl. Med. *13*, eaaz4699. https://doi.org/10.1126/scitranslmed.aaz4699.
76. LaClair, K.D., Zhou, Q., Michaelsen, M., Wefers, B., Brill, M.S., Janjic, A., Rathkolb, B., Farny, D., Cygan, M., de Angelis, M.H., et al. (2020). Congenic expression of poly-GA but not poly-PR in mice triggers selective neuron loss and interferon responses found in C9orf72 ALS. Acta Neuropathol. *140*, 121–142. https://doi.org/10.1007/s00401-020-02176-0.
77. Yu, C.H., Davidson, S., Harapas, C.R., Hilton, J.B., Mlodzianoski, M.J., Laohamonthonkul, P., Louis, C., Low, R.R.J., Moecking, J., De Nardo, D., et al. (2020). TDP-43 Triggers Mitochondrial DNA Release via mPTP to Activate cGAS/STING in ALS. Cell *183*, 636–649.e18. https://doi.org/10.1016/j.cell.2020.09.020.
78. Gerbino, V., Kaunga, E., Ye, J., Canzio, D., O'Keeffe, S., Rudnick, N.D., Guarnieri, P., Lutz, C.M., and Maniatis, T. (2020). The Loss of TBK1 Kinase Activity in Motor Neurons or in All Cell Types Differentially Impacts ALS Disease Progression in SOD1 Mice. Neuron *106*, 789–805.e5. https://doi.org/10.1016/j.neuron.2020.03.005.
79. Marques, C., Held, A., Dorfman, K., Sung, J., Song, C., Kavuturu, A.S., Aguilar, C., Russo, T., Oakley, D.H., Albers, M.W., et al. (2024). Neuronal STING activation in amyotrophic lateral sclerosis and frontotemporal dementia. Acta Neuropathol. *147*, 56. https://doi.org/10.1007/s00401-024-02688-z.
80. Izrael, M., Slutsky, S.G., and Revel, M. (2020). Rising Stars: Astrocytes as a Therapeutic Target for ALS Disease. Front. Neurosci. *14*, 824. https://doi.org/10.3389/fnins.2020.00824.
81. Guttenplan, K.A., Weigel, M.K., Adler, D.I., Couthouis, J., Liddelow, S.A., Gitler, A.D., and Barres, B.A. (2020). Knockout of reactive astrocyte activating factors slows disease progression in an ALS mouse model. Nat. Commun. *11*, 3753. https://doi.org/10.1038/s41467-020-17514-9.
82. Huang, M., Liu, Y.U., Yao, X., Qin, D., and Su, H. (2024). Variability in SOD1-associated amyotrophic lateral sclerosis: geographic patterns, clinical heterogeneity, molecular alterations, and therapeutic implications. Transl. Neurodegener. *13*, 28. https://doi.org/10.1186/s40035-024-00416-x.
83. Fu, J., and Taubman, M.B. (2010). Prolyl hydroxylase EGLN3 regulates skeletal myoblast differentiation through an NF-kappaB-dependent pathway. J. Biol. Chem. *285*, 8927–8935. https://doi.org/10.1074/jbc.M109.078600.
84. Xue, J., Li, X., Jiao, S., Wei, Y., Wu, G., and Fang, J. (2010). Prolyl hydroxylase-3 is down-regulated in colorectal cancer cells and inhibits IKKbeta independent of hydroxylase activity. Gastroenterology *138*, 606–615. https://doi.org/10.1053/j.gastro.2009.09.049.
85. Klotzsche-von Ameln, A., Muschter, A., Mamlouk, S., Kalucka, J., Prade, I., Franke, K., Rezaei, M., Poitz, D.M., Breier, G., and Wielockx, B. (2011). Inhibition of HIF prolyl hydroxylase-2 blocks tumor growth in mice through the antiproliferative activity of TGFβ. Cancer Res. *71*, 3306–3316. https://doi.org/10.1158/0008-5472.CAN-10-3838.
86. Alexander, G.M., Erwin, K.L., Byers, N., Deitch, J.S., Augelli, B.J., Blankenhorn, E.P., and Heiman-Patterson, T.D. (2004). Effect of transgene copy number on survival in the G93A SOD1 transgenic mouse model of ALS. Brain Res. Mol. Brain Res. *130*, 7–15. https://doi.org/10.1016/j.molbrainres.2004.07.002.
87. Swinnen, B., Bento-Abreu, A., Gendron, T.F., Boeynaems, S., Bogaert, E., Nuyts, R., Timmers, M., Scheveneels, W., Hersmus, N., Wang, J., et al. (2018). A zebrafish model for C9orf72 ALS reveals RNA toxicity as a pathogenic mechanism. Acta Neuropathol. *135*, 427–443. https://doi.org/10.1007/s00401-017-1796-5.
88. Carpenter, A.E., Jones, T.R., Lamprecht, M.R., Clarke, C., Kang, I.H., Friman, O., Guertin, D.A., Chang, J.H., Lindquist, R.A., Moffat, J., et al. (2006). CellProfiler: image analysis software for identifying and quantifying cell phenotypes. Genome Biol. *7*, R100. https://doi.org/10.1186/gb-2006-7-10-r100.
89. Wolf, F.A., Angerer, P., and Theis, F.J. (2018). SCANPY: large-scale single-cell gene expression data analysis. Genome Biol. *19*, 15. https://doi.org/10.1186/s13059-017-1382-0.
90. Wolock, S.L., Lopez, R., and Klein, A.M. (2019). Scrublet: Computational Identification of Cell Doublets in Single-Cell Transcriptomic Data. Cell Syst. *8*, 281–291.e9. https://doi.org/10.1016/j.cels.2018.11.005.
91. Davie, K., Janssens, J., Koldere, D., De Waegeneer, M., Pech, U., Kreft, Ł., Aibar, S., Makhzami, S., Christiaens, V., Bravo González-Blas, C., et al. (2018). A Single-Cell Transcriptome Atlas of the Aging Drosophila Brain. Cell *174*, 982–998.e20. https://doi.org/10.1016/j.cell.2018.05.057.
92. Love, M.I., Huber, W., and Anders, S. (2014). Moderated estimation of fold change and dispersion for RNA-seq data with DESeq2. Genome Biol. *15*, 550. https://doi.org/10.1186/s13059-014-0550-8.
93. Mi, H., Muruganujan, A., Ebert, D., Huang, X., and Thomas, P.D. (2019). PANTHER version 14: more genomes, a new PANTHER GO-slim and improvements in enrichment analysis tools. Nucleic Acids Res. *47*, D419–D426. https://doi.org/10.1093/nar/gky1038.
94. Elizarraras, J.M., Liao, Y., Shi, Z., Zhu, Q., Pico, A.R., and Zhang, B. (2024). WebGestalt 2024: faster gene set analysis and new support for metabolomics and multi-omics. Nucleic Acids Res. *52*, W415–W421. https://doi.org/10.1093/nar/gkae456.
95. Martin, M. (2011). Cutadapt Removes Adapter Sequences From High-Throughput Sequencing Reads. EMBnet. j. *17*, 10. https://doi.org/10.14806/ej.17.1.200.
96. Morgan, M., Lawrence, M., and Aders, S. (2009). ShortRead: Base Classes and Methods for High-Throughput Short-Read Sequencing Data.
97. Langmead, B., and Salzberg, S.L. (2012). Fast gapped-read alignment with Bowtie 2. Nat. Methods *9*, 357–359. https://doi.org/10.1038/nmeth.1923.
98. Dobin, A., Davis, C.A., Schlesinger, F., Drenkow, J., Zaleski, C., Jha, S., Batut, P., Chaisson, M., and Gingeras, T.R. (2013). STAR: ultrafast universal RNA-seq aligner. Bioinformatics *29*, 15–21. https://doi.org/10.1093/bioinformatics/bts635.
99. Li, H., Handsaker, B., Wysoker, A., Fennell, T., Ruan, J., Homer, N., Marth, G., Abecasis, G., and Durbin, R.; 1000 Genome Project Data Processing Subgroup (2009). The Sequence Alignment/Map format and

SAMtools. Bioinformatics *25*, 2078–2079. https://doi.org/10.1093/bioinformatics/btp352.

100. Liao, Y., Smyth, G.K., and Shi, W. (2014). featureCounts: an efficient general purpose program for assigning sequence reads to genomic features. Bioinformatics *30*, 923–930. https://doi.org/10.1093/bioinformatics/btt656.
101. Risso, D., Schwartz, K., Sherlock, G., and Dudoit, S. (2011). GC-content normalization for RNA-Seq data. BMC Bioinf. *12*, 480. https://doi.org/10.1186/1471-2105-12-480.
102. Robinson, M.D., and Smyth, G.K. (2007). Moderated statistical tests for assessing differences in tag abundance. Bioinformatics *23*, 2881–2887. https://doi.org/10.1093/bioinformatics/btm453.
103. Braems, E., Bercier, V., Van Schoor, E., Heeren, K., Beckers, J., Fumagalli, L., Dedeene, L., Moisse, M., Geudens, I., Hersmus, N., et al. (2022). HNRNPK alleviates RNA toxicity by counteracting DNA damage in C9orf72 ALS. Acta Neuropathol. *144*, 465–488. https://doi.org/10.1007/s00401-022-02471-y.
104. Dittlau, K.S., Chandrasekaran, A., Freude, K., and Van Den Bosch, L. (2024). Generation of Human Induced Pluripotent Stem Cell (hiPSC)-Derived Astrocytes for Amyotrophic Lateral Sclerosis and Other Neurodegenerative Disease Studies. Bio. Protoc. *14*, e4936. https://doi.org/10.21769/BioProtoc.4936.
105. Mizielinska, S., Grönke, S., Niccoli, T., Ridler, C.E., Clayton, E.L., Devoy, A., Moens, T., Norona, F.E., Woollacott, I.O.C., Pietrzyk, J., et al. (2014). C9orf72 repeat expansions cause neurodegeneration in Drosophila through arginine-rich proteins. Science *345*, 1192–1194. https://doi.org/10.1126/science.1256800.
106. Doench, J.G., Fusi, N., Sullender, M., Hegde, M., Vaimberg, E.W., Donovan, K.F., Smith, I., Tothova, Z., Wilen, C., Orchard, R., et al. (2016). Optimized sgRNA design to maximize activity and minimize off-target effects of CRISPR-Cas9. Nat. Biotechnol. *34*, 184–191. https://doi.org/10.1038/nbt.3437.
107. Swiech, L., Heidenreich, M., Banerjee, A., Habib, N., Li, Y., Trombetta, J., Sur, M., and Zhang, F. (2015). In vivo interrogation of gene function in the mammalian brain using CRISPR-Cas9. Nat. Biotechnol. *33*, 102–106. https://doi.org/10.1038/nbt.3055.
108. Batiuk, M.Y., Martirosyan, A., Wahis, J., de Vin, F., Marneffe, C., Kusserow, C., Koeppen, J., Viana, J.F., Oliveira, J.F., Voet, T., et al. (2020). Identification of region-specific astrocyte subtypes at single cell resolution. Nat. Commun. *11*, 1220. https://doi.org/10.1038/s41467-019-14198-8.
109. van Bruggen, D., Agirre, E., and Castelo-Branco, G. (2017). Single-cell transcriptomic analysis of oligodendrocyte lineage cells. Curr. Opin. Neurobiol. *47*, 168–175. https://doi.org/10.1016/j.conb.2017.10.005.
110. Marques, S., Zeisel, A., Codeluppi, S., van Bruggen, D., Mendanha Falcão, A., Xiao, L., Li, H., Häring, M., Hochgerner, H., Romanov, R.A., et al. (2016). Oligodendrocyte heterogeneity in the mouse juvenile and adult central nervous system. Science *352*, 1326–1329. https://doi.org/10.1126/science.aaf6463.
111. Rué, L., Oeckl, P., Timmers, M., Lenaerts, A., van der Vos, J., Smolders, S., Poppe, L., de Boer, A., Van Den Bosch, L., Van Damme, P., et al. (2019). Reduction of ephrin-A5 aggravates disease progression in amyotrophic lateral sclerosis. Acta Neuropathol. Commun. *7*, 114. https://doi.org/10.1186/s40478-019-0759-6.
112. Benjamini, Y., and Hochberg, Y. (1995). Controlling the False Discovery Rate: A Practical and Powerful Approach to Multiple Testing. J. Roy. Stat. Soc. B *57*, 289–300. https://doi.org/10.1111/j.2517-6161.1995.tb02031.x.

STAR★METHODS

KEY RESOURCES TABLE

REAGENT or RESOURCE	SOURCE	IDENTIFIER
Antibodies		
SV2	Developmental Studies Hybridoma Bank	RRID: AB_2315387
Neurofilament-L	Cell Signaling	RRID: AB_823575
AF555 α-Bungarotoxin	Invitrogen	RRID: AB_2617152
AF647 Isolectin IB4	Life technologies	Cat#I32450
GFAP	Sigma	RRID: AB_477010
STING	Cell Signaling	RRID: AB_2732796
Oct4	Santa Cruz	RRID: AB_2167703
TRA-1-60 (IgM)	Cell Signaling	RRID: AB_2119059
Sox2	Abcam	RRID: AB_2341193
SSEA4	Santa Cruz	RRID: AB_628289
Nanog	Thermo Scientific	RRID: AB_2539867
SOD1	Enzo	RRID: AB_2039583
Calnexin	Enzo	RRID: AB_11178981
VIM	Abcam	RRID: AB_10562134
AQP4	Abcam	RRID: AB_307299
SOX9	R&D Systems	RRID: AB_2194160
TRA-1-81(IgM)	Cell Signaling	RRID: AB_2119060
AF488 anti-Rabbit	Invitrogen	RRID: AB_2576217
AF555 anti-Mouse (IgM)	Invitrogen	RRID: AB_2535847
AF555 anti-Mouse (IgG)	Invitrogen	RRID: AB_141780
AF488 anti-Rabbit	Invitrogen	RRID: AB_2535792
AF555 anti-Mouse (IgG)	Invitrogen	RRID: AB_2536180
Critical commercial assays		
mMESSAGE mMACHINE™ T3 Transcription Kit	Invitrogen	Cat#AM1348
mMESSAGE mMACHINE™ T7 ULTRA Transcription Kit	Invitrogen	Cat#AM1345
MEGAclear™ Transcription Clean-Up Kit	Invitrogen	Cat#AM1908
PureLink PCR Purification Kit	Invitrogen	Cat#K310001
GenElute™ Total RNA Purification Kit	Sigma-Aldrich	Cat#RNB100
SuperScript™ III First-Strand Synthesis System kit	Invitrogen	Cat#18080051
TaqMan hPSC Scorecard® 384-well plate	Applied Biosystems	Cat#A15870
TaqMan® SNP Genotyping Assay	Life technologies	N/A
RNeasy kit	Qiagen	Cat#74104
micro BCA kit	Pierce Biotechnology	Cat#23235
RNAscope Multiplex Fluorescent Reagent Kit v2	Advanced Cell Diagnostics	N/A
Illumina Stranded mRNA Sample Prep Kit v02	Illumina	Cat#1000000124518
Chemicals, peptides, and recombinant proteins		
Asp718 restriction enzyme	Thermo Scientific	Cat#ER0901
AgeI restriction enzyme	Thermo Scientific	Cat#ER1461
Y-27632	Gibco	Cat#SCM075
Alt-R™ S.p. Cas9 Nuclease V3	IDT	Cat#1081058
RevitaCell	Gibco	Cat#A2644501
LDN-193189	Stemgent	Cat#04-0074-02
SB431542	Tocris	Cat#1614

(*Continued on next page*)

Continued

REAGENT or RESOURCE	SOURCE	IDENTIFIER
L-glutamine	Thermo Scientific	Cat#25030-024
N-2 supplement	Gibco	Cat#17502-048
B-27^{TM} without vitamin A	Gibco	Cat#12587-010
FGF-2	PeproTech	Cat#450-33
EGF	ProSpec	Cat#CYT-217
non-essential amino acids	Gibco	Cat#11140050
ascorbic acid	Sigma-Aldrich	Cat#A4403
IGF-1	Peprotech	Cat#100-11
human Activin A	Gibco	Cat#PHC9564
Heregulinβ1	Peprotech	Cat#100-03
sodium pyruvate	Gibco	Cat#11360-070
IL-1α	Bio-techne	Cat#200-LA-010
TNFα	Bio-techne	Cat#210-TA-020
C1q	Sigma-Aldrich	Cat#204876
normal donkey serum	Sigma-Aldrich	Cat#D9663
TriPure	Roche	Cat#11667157001
Deposited data		
Murine snRNA-seq dataset	This Paper	GEO: GSE219201
iPSC-Astrocyte RNA-seq dataset	This Paper	GEO: GSE260913
Experimental models: Cell lines		
SOD1^{A4A} iPSCs	Kiskinis et al.[57]	N/A
SOD1^{A4V} iPSCs	Kiskinis et al.[57]	N/A
SOD1^{A4V}/EGLN2$^{-/-}$ iPSCs	This paper	N/A
Experimental models: Organisms/strains		
SOD1^{G93A} mice	The Jackson Laboratory	RRID: IMSR_JAX:002726
Egln2$^{-/-}$ mice	Aragones et al.[9]	N/A
AB zebrafish	European Zebrafish Resource Center (EZRC)	RRID: ZFIN_ZDB-GENO-960809-7
Oligonucleotides		
egln2 AMO TATACATCGCCTCTCACTCACCT	Genetools	N/A
Ctrl AMO CCTCTTACCTCAGTTACAATTTAT	Genetools	N/A
Alt-R^{TM} CRISPR-Cas9 sgRNA ACGAAGACCCTGGTAACTGA	IDT	N/A
Stmn2 RNAScope probe	Advanced Cell Diagnostics	Cat#Mm-Stmn2-C2
Syp RNAScope probe	Advanced Cell Diagnostics	Cat#Mm-Syp-C3
Primers for RT-PCR and qRT-PCR: see Tables S7 and S8		N/A
Recombinant DNA		
SOD1^{WT} plasmid	Lemmens et al.[32]	N/A
SOD1^{G93A} plasmid	Lemmens et al.[32]	N/A
91S plasmid	Swinnen et al.[87]	N/A
GFP plasmid	Origene	Cat#PS100010
Software and algorithms		
ImageJ	NIH	RRID: SCR_003070
SnapGene	Dotmatics	RRID: SCR_015052
ICE tool	Synthego	RRID: SCR_024508
CRISPOR tool	Tefor Infrastructure	RRID: SCR_015935
TaqMan Genotyper Software	Life Technologies	N/A
Cytosure	OGT	N/A

(*Continued on next page*)

Continued

REAGENT or RESOURCE	SOURCE	IDENTIFIER
CellProfiler Image Analysis Software	Carpenter et al.[88]	RRID: SCR_007358
LUCIA software version 4.60	Laboratory Imaging	N/A
cellranger count v5.0.2	10X Genomics	RRID: SCR_023221
Scanpy v1.8.1	Wolf et al.[89]	RRID: SCR_018139
Scrublet v0.2.2	Wolock et al.[90]	RRID: SCR_018098
Scope	Davie et al.[91]	RRID: SCR_017454
DESeq2	Love et al.[92]	RRID: SCR_015687
PANTHER v14.1	Mi et al.[93]	RRID: SCR_004869
WebGestalt 2024	Elizarraras et al.[94]	RRID: SCR_006786
FastX 0.0.14	Illumina	RRID: SCR_005534
Cutadapt 3.2	Martin et al.[95]	RRID: SCR_011841
ShortRead 1.58.0	Morgan et al.[96]	RRID: SCR_006813
Bowtie2 2.4.5	Langmead et al.[97]	RRID: SCR_016368
STAR aligner v2.5.2b	Dobin et al.[98]	RRID: SCR_004463
Samtools 1.15.1	Li et al.[99]	RRID: SCR_002105
featureCounts 1.5.3	Liao et al.[100]	RRID: SCR_002105
EDASeq 2.32	Risso et al.[101]	RRID: SCR_006751
EdgeR 3.42.4	Robinson et al.[102]	RRID: SCR_012802
Graphpad Prism v8.0	Graphpad	RRID: SCR_002798

EXPERIMENTAL MODEL AND STUDY PARTICIPANT DETAILS

Zebrafish

All experiments were approved by the Ethics Committee of KU Leuven (P112/2021). Zebrafish (AB strain, RRID: ZFIN_ZDB-GENO-960809-7) embryos were kept in a 28°C incubator. Micro-injection of 1000 ng/μL *SOD1*^{WT} and *SOD1*^{G93A} RNA or 181 ng/μL 91 (91S) *C9orf72* hexanucleotide repeats and *GFP* RNA, as specified before,[32,103] and 0.1 mM *egln2* AMO was done in 1–2 cell stage zebrafish oocytes. Motor axons were assessed with an SV2 staining at 30 hpf. The sexual differentiation of zebrafish occurs later on so gender is not relevant.

Mice

All animal experiments were approved by the Ethical Committee of KU Leuven (P020/2020). Mice were housed at the KU Leuven animal facilities with a 12 h light-dark cycle at a temperature of 20°C. Standard rodent chow and water was provided *ad libitum*. SOD1^{G93A} mice overexpressing human mutant *SOD1* (glycine to alanine substitution at codon 93) were purchased from The Jackson Laboratory (Maine, United States of America (US)) (stock number: 002726, RRID: IMSR_JAX:002726) and maintained on a C57BL/6 background. *Egln2*$^{-/-}$ mice were generated previously[33] and backcrossed for seven generations to obtain a pure C57BL/6 background. *Egln2*$^{-/-}$ mice were intercrossed with *SOD1*^{G93A} mice to generate *SOD1*^{G93A}/*Egln2*$^{-/-}$ and *SOD1*^{G93A}/*Egln2*$^{+/-}$ mice and investigated together with their *SOD1*^{G93A}/*Egln2*$^{+/+}$ littermate controls. Mice were followed-up over their lifespan and additional analyses such as motor neuron count, NMJ quantification and snRNA-seq were performed at P110. For all experiments, littermate controls and both male and female mice were used.

iPSCs

All experiments were approved by the Ethical Committee of UZ Leuven (S50354). iPSCs from a female ALS patient carrying a *SOD1*^{A4V} and its isogenic control (*SOD1*^{A4A}) were generated previously by Kiskinis et al.[57] and kindly provided by prof. K. Eggan (Harvard University, Cambridge, US). iPSCs were cultured on Geltrex (A1413201, Gibco, Waltham, US) in Complete Essential 8 medium (A1517001, Gibco) with 1% penicillin/streptomycin (15070063, Gibco) in a humidified 5% CO_2 incubator at 37°C. A CRISPR-Cas9 mediated knock-out of *EGLN2* was generated in *SOD1*^{A4V} iPSCs as explained in the method details section. *SOD1*^{A4A}, *SOD1*^{A4V} and *SOD1*^{A4V}/*EGLN2*$^{-/-}$ iPSCs were differentiated into astrocytes using a previously established protocol,[104] further explained in the method details section. Transcriptomic and immunocytochemical analysis were performed after 6 weeks of maturation (d+41).

METHOD DETAILS

Zebrafish *DNA constructs and AMO*

Human cDNA of *SOD1*^{WT} and *SOD1*^{G93A} in the pCLneo vector were kindly provided by R.H. Brown Jr (UMass Chan Medical School, Worcester, US). SOD1 was cloned in the pBCM vector behind a T3 promoter and linearized using Asp718 restriction enzyme (ER0901, Thermo Scientific, Waltham, US). Plasmids containing 91 (91S) *C9orf72* hexanucleotide repeats under a T7 promotor were obtained and adapted as described previously.[87,105] The GFP control plasmid construct (PS100010, Origene, Rockville, USA) was digested with AgeI restriction enzyme (ER1461, Thermo Scientific). RNA was transcribed from DNA using mMESSAGE mMACHINE T3 Transcription Kit (AM1348, Invitrogen, Waltham, US) or mMESSAGE mMACHINE T7 ULTRA Transcription Kit (AM1345, Invitrogen) and purified using the MEGAclear Transcription Clean-Up Kit (AM1908, Invitrogen). Antisense morpholino oligonucleotides (AMOs) were designed and obtained from Gene Tools (Philomath, US): control AMO (sequence: CCTCTTACCTCAG TTACAATTTAT) and *egln2* E2I2 AMO (sequence: TATACATCGCCTCTCACTCACCT).

Mice disease onset and survival

Disease onset was determined by bodyweight and rotarod performance. Disease onset was considered as the last time point at which the mouse maintained 90% of its peak body weight or at the last time point at which the latency to fall on the rotarod (Ugo Basile, Gemonio, Italy) was longer than 150 s at a constant speed of 15 rpm. Survival was determined by the loss of righting reflex within 20 s. This time point was considered as humane endpoint, whereupon the mouse was sacrificed.

Mice motor neuron counts

Mice were anesthetized using 10% Dolethal (Vétoquinol, Lure, France) and transcardially perfused with 1X PBS (806552, Sigma-Aldrich, Saint-Louis, US) followed by perfusion with 4% paraformaldehyde (PFA). Lumbar spinal cords were harvested, post-fixed with 4% PFA overnight at 4°C and dehydrated for 48 h in a 30% sucrose solution at 4°C. Following embedding in Optimal Cutting Temperature (O.C.T.) (00411243, VWR, Radnor, US) compound mounting medium for cryometry, the samples were stored at −80°C until further processing. 20 μm cryosections were obtained and every tenth section was stained with 2X thionin solution to visualize the motor neuron cell bodies in the ventral horn. Briefly, cryosections were fixed for 1 min in 100% ethanol in a cryochamber and subsequently washed for 15 s in distilled water, stained with 2X thionin during 45 s, washed twice in distilled water and dehydrated in 70%, 90% and 100% ethanol for 30 s each. Histological sections were cleared with Histoclear solution for 1 min and mounted using PerTex (00801, Histolab, Västra Frölunda, Sweden). A minimum of ten spinal cord sections for each mouse were analyzed. Images were taken using the Zeiss Imager M1 microscope (Carl Zeiss Inc., Oberkochen, Germany). Neuron size and number was quantified using ImageJ (RRID: SCR_003070) and were normalized to the ventral horn size of the respective section and multiplied by the ventral horn size of a non-transgenic mouse (300,000 μm^2).

Generation and quality control of EGLN2 knock-out iPSCs

Generation of EGLN2 knock-out iPSC line using CRISPR-Cas9

To perform electroporation, iPSCs were incubated at 37°C for at least 1 h in mTESR1 medium (85850, Stemcell technologies, Vancouver, Canada) containing 10 μM Y-27632 Rho-Associated Kinase (ROCK) inhibitor (ROCKi) (SCM075, Gibco). Next, the colonies were dissociated to single cells by incubation with accutase (A6964, Sigma-Aldrich) at 37°C for 15–20 min. Approximately 1.2 x 10^5 cells were resuspended in 100 μL optimum and mixed with Ribonucleoprotein (RNP) form of CRISPR-Cas9 system composed of Cas9 protein (1081058, Alt-R S.p. Cas9 Nuclease V3, IDT, Newark, US) and a sgRNA (Alt-R CRISPR-Cas9 sgRNA, IDT) with the following sequence: ACGAAGACCCTGGTAACTGA. After nucleofection using the Nepagene electroporator with the following settings; poring pulse (voltage 125v, pulse length 5 msec, pulse interval 50 msec, number of pulses 2, decay rate of 10%, and polarity set at +) and transfer pulse (voltage 20 v, pulse length 50 msec, pulse interval 50 msec, number of pulses 5, decay rate of 40%, and polarity set at+/−), cells were immediately collected in mTESR1 containing ROCKi, re-plated on plates coated with BD Matrigel (356234, BD, Franklin Lakes, US) and placed in the incubator. The day after, medium was switched to E8 Flex supplemented with 10 μM ROCKi. After 10–15 days single colonies were picked using a colony picker tool (Fine Science Tools, Heidelberg, Germany) under a microscope placed in a class I biological safety cabinet. Colonies were genotyped via sequencing the target region using Q5 2x mastermix (M0492S, New England BioLabs, Ipswich, US). Amplicons were purified using PureLink PCR Purification Kit (K310001, Invitrogen) prior to Sanger sequencing (Europhins Genomics, Ebersberg, Germany). Sanger sequencing results were analyzed using SnapGene (RRID: SCR_015052) version 6.1.1 software and Synthego ICE tool (RRID: SCR_024508). Quality control including off-target analysis, immunofluorescence, embryoid body (EB) formation scorecard analysis, single nucleotide polymorphism (SNP) profiling and array-comparative genomic hybridization (array-CGH) were performed as described below.

Off-target analysis

Prediction of off-target sites was performed by using CRISPOR tool (http://crispor.tefor.net/, RRID: SCR_015935). Five predicted off target sites with the highest Cutting Frequency Determination (CFD) scores were selected.[106] Off target regions were PCR amplified and subjected to Sanger sequencing. Sanger sequencing results were analyzed using SnapGene version 6.1.1 software and Synthego ICE tool. This revealed no effect on any of the predicted off target sites.

Immunofluorescence analysis of pluripotent markers

Cells were fixed with 4% PFA for 10 min, washed with PBS and permeabilized with 0.1% Triton X- in PBS, followed by 30 min blocking with 5% goat serum in PBS (Dako, Glostrup, Denmark). Cells were stained overnight at 4°C with primary antibodies (Table S6) and washed three times for 5 min with 0.1% Triton X- in PBS. Next, cells were incubated for 60 min at room temperature with the appropriate secondary antibodies (Table S6), washed three times and stained with Hoechst 33342 (14533, Sigma-Aldrich, 1:2000 dilution). Coverslips were mounted using Prolong Gold antifade reagent (P36930, Invitrogen) on superfrost microscope slides (10457673, ThermoFisher Scientific). Images were taken using the Axioimager Z.1 fluorescence microscope (Carl Zeiss Inc.).

Embryoid body (EB) formation and scorecard analysis

To make EBs, iPSCs were washed with PBS and incubated 1 min with EDTA. Cells were harvested and counted. Approximately one million cells were resuspended in 1 mL Essential 6 medium (A1516401, Gibco) and 10 μL RevitaCell supplement (A2644501, Gibco), transferred to one well of Ultra-Low Attachment 24-well plates (CLS3471, Corning, New York, US) and maintained for 7 days with half medium changes every other day. The rest of the cells were frozen as dry pellet as Day 0 control. EBs were collected after 7 days for RNA isolation using GenElute Total RNA Purification Kit (RNB100, Sigma-Aldrich) and cDNA synthesis using SuperScript III First-Strand Synthesis System kit (18080051, Invitrogen). cDNA samples were mixed with water and TaqMan Gene Expression Master Mix (4369016, Applied Biosystems, Waltham, US) and loaded to a TaqMan hPSC Scorecard 384-well plate (A15870, Applied Biosystems). Results were analyzed with the hPSC Scorecard analysis software.

Single nucleotide polymorphism (SNP) profiling

SNP profiling was performed using TaqMan SNP Genotyping Assay (Life Technologies, Carlsbad, US) customized for genotyping SNPs in each sample. Custom made TaqMan SNP Genotyping Assay (384-well plate) was loaded using 2.5 μL 2x TaqMan GTXpress Master Mix mixed with 2.5 μL genomic DNA (4 ng/μL) per well. Results were analyzed by TaqMan Genotyper Software (Life Technologies) and revealed no differences between the *SOD1*^{A4V} iPSC baseline and CRISPR-Cas9 edited *SOD1*^{A4V}/*EGLN2*$^{-/-}$ iPSC line.

Array-comparative genomic hybridization (array-CGH)

Genomic DNA samples were extracted using PureLink Genomic DNA kit (Invitrogen). Array-CGH was performed in UZ Leuven, Centrum Menselijke Erfelijkheid (CME). Results were analyzed using CytoSure interpret software. 5p.11 and 12 duplication in chromosome 5 were detected in *SOD1*^{A4V} and *SOD1*^{A4V}/*EGLN2*$^{-/-}$ iPSCs, 20q.11 duplication was detected in chromosome 20 of SOD1^{A4V} iPSCs and 20q.11 triplication was detected in chromosome 20 of *SOD1*^{A4V}/*EGLN2*$^{-/-}$ iPSCs.

Generation of iPSC-derived astrocytes

iPSCs were differentiated in mature astrocytes as described previously.[104] In short, iPSCs were dissociated with collagenase type IV (10780004, Gibco) and cultured in Corning ultra-low attachment plates with neuronal induction medium (NIM) consisting of Complete Essential 8 medium with 1% penicillin/streptomycin supplemented with 0.1 μM LDN-193189 (04–0074-02, Stemgent, Beltsville, US) and 10 μM SB431542 (1614, Tocris, Bristol, UK) for the first week to support neuronal induction to form EBs. NIM was changed on day 1, 2 and 4. On day 7, EBs were plated on Geltrex-coated plates in neuronal maturation medium (NMM) consisting of 50% DMEM/F12 (11330032, Gibco) and 50% Neurobasal medium (21103049, Gibco) with 1% L-glutamine (25030–024, Thermo Scientific), 1% penicillin/streptomycin, 1% *N*-2 supplement (17502–048, Gibco) and 2% B-27 without vitamin A (12587–010, Gibco) supplemented with 10 ng/mL recombinant murine fibroblast growth factor (FGF)-2 (450–33, PeproTech, Cranbury UK), 10 ng/mL recombinant human epidermal growth factor (EGF) (CYT-217, ProSpec, Rehivit, Israel), 0.1 μM LDN-193189 and 10 μM SB431542 to allow neural rosette formation and induce neural progenitor cell (NPC) expansion. NMM was changed every other day and NPCs were passaged using accutase when 100% confluency was reached. On day 16, neuronal NMM was switched to astrocyte differentiation medium (ADM) consisting of 90% Neurobasal medium, 1% penicillin/streptomycin, 1% *N*-2 supplement, 1% non-essential amino acids (11140050, Gibco) and 0.8 μM ascorbic acid (A4403, Sigma-Aldrich) supplemented with 10 ng/mL FGF-2, 200 ng/mL recombinant human insulin like growth factor (IGF)-1 (100–11, Peprotech), 10 ng/mL human Activin A (PHC9564, Gibco) and 10 ng/mL recombinant human Heregulinβ1 (100–03, Peprotech). ADM was changed every other day until day 25 to convert NPCs to astrocyte progenitor cells (APCs). On day 25 (d25/d+0), a glial switch occured to commence the astrocyte maturation, which took an additional 4 weeks. APCs were plated on Geltrex-coated plates for expansion and maturation in astrocyte maturation medium (AMM) consisting of 50% DMEM/F12, 50% Neurobasal medium, 1% non-essential amino acids, 1% *N*-2 supplement, 1% L-glutamine, 1% penicillin/streptomycin, 2% fetal bovine serum (FBS) (10270106, Gibco), 0.8 μM ascorbic acid, and 1% sodium pyruvate (Gibco, 11360–070) supplemented with 200 ng/mL IGF-1, 10 ng/mL Activin A and 10 ng/mL Heregulinβ1 which was changed every other day. After 36 days (d+36) of maturation, mature astrocytes were plated in Geltrex-coated 6-well plates at 300,000 cells per well. At day 40, after recovery, cells were treated with 3 ng/mL IL-1α (200-LA-010, Bio-techne, Minneapolis, US), 30 ng/mL TNFα (210-TA-020, Bio-techne) and 400 ng/mL C1q (204876, Sigma-Aldrich) in AMM medium without FBS. After 24h treatment, cells were collected with accutase for RNA extraction and sequencing or fixed with 4% PFA for immunocytochemistry.

Immunofluorescence

Mice

Mice were anesthesized using 10% Dolethal and transcardially perfused with PBS followed by perfusion with 4% PFA. Lumbar spinal cords were harvested from P110 mice, post-fixed with 4% PFA overnight at 4°C and dehydrated over 48 h in a 30% sucrose solution at 4°C. Following embedding in O.C.T. compound mounting medium samples were stored at −80°C until further processing.

Gastrocnemius muscles were harvested from P110 mice, snap-frozen in liquid-nitrogen cooled isopentane, embedded in O.C.T and stored at −80°C until further processing. 20 μm longitudinal (gastrocnemius muscle) or transversal (lumbar spinal cord) sections were obtained and processed for immunostaining. In brief, sections were blocked for 1 h in 10% normal donkey serum (D9663, Sigma-Aldrich), PBS-T (PBS +0.1% Triton X-100) and incubated subsequently for 1 h at room temperature with the required antibodies (Table S6) dissolved in PBS-T supplemented with 10% normal donkey serum. Images were taken with a Leica TCS SP8 confocal laser scanning microscope (Leica Microsystems Heidelberg GmbH, Manheim, Germany) or a Zeiss Axio Scan 7 microsope ((Carl Zeiss Inc.) and analyzed with ImageJ or CellProfiler Image Analysis Software (RRID: SCR_007358).[88]

Zebrafish

Zebrafish were collected at 30 hpf and fixed overnight with 4% PFA at 4°C. Fixation was followed by permeabilization with acetone for 1 h at −20°C, blocking with 1% bovine serum albumin (BSA), 1% dimethyl sulfoxide (DMSO) PBS for 1 h at RT and immunostaining with primary mouse anti-synaptic vesicle glycoprotein 2 (SV2) (Table S6) in 1%DMSO/PBS for 3 h at RT. Embryos were incubated overnight at 4°C with secondary Alexa Fluor 555 anti-mouse antibody (Table S6) in 1% DMSO/PBS. Stained zebrafish embryos were analyzed with a Leica DM 3000 LED fluorescence microscope using LUCIA software version 4.60 (Laboratory Imaging). Fish were scored on axonal length and abnormal branching of ventral root projections using a standardized method. Axonal length was measured from the 8th up to the 12th axon on one side in 15 fish per condition in each experiment. Abnormal branching was scored from the 8th up to the 17th axon on both sides. Branching was considered abnormal when at least two out of 20 axons were branched at or above the ventral edge of the notochord.

iPSC-derived astrocytes

iPSC-derived astrocytes were fixed at d+41 with 4% PFA. After fixation, cells were blocked for 1 h in 5% normal donkey serum, PBS-T and incubated subsequently for 1 h at room temperature with the required antibodies (Table S6) dissolved in PBS-T supplemented with 2% normal donkey serum. Images were taken with a Leica TCS SP8 confocal laser scanning microscope and analyzed with ImageJ.

RNA isolation, qRT-PCR and RT-PCR

Mice

Mice were anesthetized using 10% Dolethal and transcardially perfused using 1X PBS. Tissues were harvested and immediately stored at −80°C until further processing. Total RNA was extracted using TriPure (11667157001, Roche, Basel, Switzerland) and isopropanol purification. cDNA was synthesized using the Superscript III First-strand Synthesis Mastermix kit. qRT-PCR reactions were performed on 4uL 1.25 ng/ul cDNA using SYBR green Universal PCR master mix (4309155, Invitrogen) and DNA primers (Tables S7 and S8). Samples were run in triplicate in a 96-well plate and thermal cycling was performed on a StepOne-Plus RT-PCR system using a standard amplification protocol. Data were analyzed using the delta delta Ct method. *Gapdh* was used as housekeeping.

Zebrafish

Zebrafish were collected at 30 hpf on dry ice and stored at − 80°C. Total RNA was extracted using the RNeasy kit (74104, Qiagen, Hilden, Germany) and cDNA was synthesized using the Superscript III First-strand Synthesis Mastermix kit. RT-PCR was performed using DreamTaq Green PCR Master Mix (K1081, ThermoFisher Scientific) and DNA primers (Table S7). RT-PCR products were analyzed on a 1% agarose gel and visualized using MIDORI Green staining (Nippon Genetics, Düren, Germany). qRT-PCR reactions were performed on 4uL 1.25 ng/ul cDNA using SYBR green Universal PCR master mix and DNA primers (Table S7). Samples were run in triplicate in a 96-well plate and thermal cycling was performed on a StepOne-Plus RT-PCR system (Applied Biosystems) using a standard amplification protocol. Data were analyzed using the delta delta Ct method. *Gapdh* and *Elp1* were used as housekeeping.

Western blot analysis

P110 mice were anesthetized using 10% Dolethal and transcardially perfused using 1X PBS. Tissues were harvested and immediately stored at −80°C until further processing. Protein was extracted in RIPA buffer (50mM Tris-HCl (pH7.5), 150 mM NaCl, 1% NP-40, 0.5% Na-deoxycholic acid, 0.5% SDS) supplemented with Complete EDTA-free protease inhibitor cocktail (11873580001, Roche). Lumbar spinal cord tissues were homogenized using Lysing Matrix D beads (116913050-CF, MP Biomedicals, Solon, US) and a MagNa Lyser oscillator (Roche) at 6500 rpm for 30 s, three times with 1 min intervals on ice. Next, the samples were centrifuged at 14,000 rpm for 20 min and supernatant was collected. Protein concentrations were determined using the micro BCA kit (23235, Pierce Biotechnology, Rockford, US). 30 μg sample together with reducing sample buffer (15492859, ThermoFisher Scientific) was heated for 10 min at 95°C. After separation on an SDS–polyacrylamide electrophoresis gel (12%, 90 V), samples were transferred to a polyvinylidene difluoride (PVDF) membrane (IPVH00010, Millipore, Massachusetts, US) by a semi-dry transfer apparatus (Bio-Rad, Hercules, US). Membranes were blocked with 5% milk TBS-T (10mM Tris-HCl (pH 7.5), 150mM NaCl and 1% Tween 20) for 1 h at RT and subsequently incubated with primary antibodies against human SOD1 and calnexin (Table S6) overnight at 4°C. Finally, the membranes were incubated with the appropriate secondary antibody conjugated with horseradish peroxidase (HRP) (1/5000; AgilentTechnologies (Dako)) for 1 h at RT and protein bands were visualized using enhanced chemiluminescence (ECL substrate, 32106, ThermoFisher Scientific) and an ImageQuant LAS 4000 Biomolecular Imager (GE Healthcare, Illinois, US). Band intensities were quantified using ImageJ.

Single-nuclei RNA sequencing of mice lumbar spinal cord

Single nuclei extraction

To extract nuclei from frozen mouse lumbar spinal cords, we used a slightly modified version of the protocol described previously by Swiech et al.[107] In brief, lumbar spinal cords from P110 mice were dissected and frozen immediately in precooled RNAse-free eppendorfs. Tissue was stored at −80°C until nuclei were extracted. At the day of nuclei extraction, frozen tissues were left in homogenization buffer (320 mM sucrose, 5 mM $CaCl_2$, 3 mM Mg Acetate, 10 mM Tris pH8, 0.1 mM EDTA, 0.1% Igepal/NP-40, 0.1 mM PMSF, 1 mM β-mercaptoethanol in H_2O) for 5 min on ice to prevent nuclei from breaking. Next, tissue was homogenized by 100 gentle manual strokes using a Dounce homogenizer (Sigma-Aldrich). Subsequently, a 1:1 volume of gradient medium (5 mM $CaCl_2$, 3 mM Mg Acetate, 10 mM Tris pH 8, 0.1 mM PMSF, 1 mM β-mercaptoethanol, 50% Optiprep, in water) was layered on top of the homogenized sample before ultracentrifugation (7,700 rpm for 30 min at 4°C using a SW41Ti rotor). Subsequently, the nuclei-containing pellet was resuspended in 150 μL resuspension buffer (BSA 1%, nuclease free water 340 mM, RNasin Plus 0.2 U/μL in 1X PBS). Number and quality of purified nuclei was controlled using a LUNA-FL Dual fluorescence cell counter (Logos Biosystems, Anyang-si, South Korea).

After single nuclei preparation, samples were immediately processed for the single nuclei whole transcriptome analysis (WTA). SnRNA-seq analysis was performed using 10X genomics 3′ WTA suite, according to the manufacturer recommendation. In brief, single nuclei were encapsulated in droplets for lysis and subsequent reverse transcription of polyadenylated mRNA species. After the first cDNA amplification, the library was subjected to Trueseq based library preparation to incorporate the Illumina sequencing adaptors and indices. The final library obtained at the end of the snRNA-seq workflow was sequenced on either of the Illumina Hiseq 4000 or Illumina NovaSeq6000 platforms as per the sequencing specification mentioned in the 10X scRNAseq workflow. Each lane was pooled with multiple 10X libraries which were indexed separately.

10x genomics data processing

Fastq files from 10x experiments were mapped to the mouse genome (mm10-2020-A, provided by 10x genomics) using cellranger count (RRID: SCR_023221) v5.0.2, the includeIntrons option was enabled. Filtered count matrices were loaded into Scanpy (RRID: SCR_018139) v1.8.1 and nuclei with more than 15% reads associated to mitochondrial genes or less than 250 genes expressed were filtered out, next Scrublet (RRID: SCR_018098) v0.2.2 was used to remove doublets with thresholds being determined automatically. All nuclei were combined into a single dataset for further processing, nuclei were then normalized to a total of 10000 counts and log transformed. Highly variable genes were detected using default parameters and the counts were finally scaled to unit variance with a zero mean and values greater than ten were clipped. A principal component analysis was performed, and harmony batch correction (performed via vsn-pipelines v0.25.0 [https://doi.org/10.5281/zenodo.3703108]) was used to integrate data between experiments, the number of components to use for subsequent analyses (UMAP, tSNE and Leiden clustering) was determined using the pcacv functionality of vsn-pipelines (57 PCs). Leiden clustering was performed at various resolution (0.4 -> 8.0) and marker genes were calculated using standard Scanpy functions. A combined clustering level was created by using the leiden resolution0.8 clusters as a base, and re-annotating cells from cluster 64 at resolution 4.0 as a new, final cluster. Clusters were annotated to known cell types using publicly available single-cell data[35–43,108–110] and confirmed by evaluating the expression of known cell type markers in our clusters using the online tool Scope[91] (RRID: SCR_017454). Differential gene expression was performed by first creating pseudobulk samples (summed counts) from each group of interest separated by initial sample of origin, and subsequently performing a DESeq2[92] (RRID: SCR_015687) differential analysis between genotypes, per cluster including the Experiment of origin as a covariate.

Gene ontology (GO) analysis and gene set enrichment analysis (GSEA)

GO enrichment of DEGs were performed using the PANTHER (RRID: SCR_004869) v14.1 GO biological process complete.[93] Only DEGs with $0.5 \leq \log10(FC) \leq -0.5$ and $p < 0.05$ were included. GSEA analysis was performed using WebGestalt (RRID:SCR_006786) 2024[94] on the ranked gene sets. Mitochondrially encoded genes, that could be present due to the use of a gentle lysis buffer during nuclei extraction, were excluded from both analyses.

RNAScope *in situ* hybridization

RNAscope was performed as previously described by Rué et al.[111]

Mice were anesthetized using 10% Dolethal at P110 and transcardially perfused with 1X PBS followed by perfusion with 4% PFA. Lumbar spinal cords were harvested, post-fixed with 4% PFA overnight at 4°C and dehydrated for 48 h in a 30% sucrose solution at 4°C. Following embedding in O.C.T. compound mounting medium for cryometry the samples were stored at −80°C until further processing. 20 μm cryosections, obtained using a CryoStar NX70 Cryostat, were mounted on Superfrost Plus slides. To improve attachment of the spinal cord slices on the slides, slices were post-fixed for 30 min with cold 4% PFA at 4°C, rinsed with PBS and dehydrated in 70%, 90% and 100% ethanol for 5 min each and baked for 30 min at 60°C. RNAscope *in situ* hybridization was performed as indicated by the manufacturer with the RNAscope Multiplex Fluorescent Reagent Kit v2 (Advanced Cell Diagnostics, San Francisco, US).

In brief, slides underwent an antigen retrieval step of 5 min at 98°C–104°C with a Braun Multiquick FS-3000 Steamer (Braun, Kronberg, Germany). Followed by a Protease III incubation step of 30 min at 40°C in a HybEZ Oven (Advanced Cell Diagnostics, Newark, US). RNAscope probes against Stathmin-2 (Stmn2, 1:125; RNAscope Probe Mm-Stmn2-C2; Advanced Cell Diagnostics) and Synaptophysin (Syp; 1:150; RNAscope Probe - Mm-Syp-C3; Advanced Cell Diagnostics) were used. Signal amplification was

performed as stated in the manufacturer's instructions with TSA Plus Cyanine 3 (NEL744001KT, PerkinElmer, Waltham, US, diluted 1:500) and TSA Plus Fluorescein (NEL741001KT, PerkinElmer, diluted 1:750). Nuclear counterstain was performed with Hoechst 33342 (5 μg/mL) and slides were finally mounted with ProLong Gold antifade reagent. Images of the ventral horns were obtained with a Leica TCS SP8 confocal laser scanning microscope with an HC PL APO CS2 20x/0.75 dry lens and a pinhole of 0.5 Airy Units.

RNA sequencing of iPSC-derived astrocytes

RNA extraction and quality control

iPSC-derived astrocytes were collected at d+41 with accutase and total RNA was extracted using the RNeasy kit. RNA concentration and purity were determined spectrophotometrically using the Nanodrop ND-8000 (Nanodrop Technologies, Wilmington, US) and RNA integrity and concentration were assessed using a Fragment Analyzer SS-RNA kit (Agilent, Santa Clara, US).

Library preparation

Per sample, 250 ng of total RNA was used as input. Using the Illumina Stranded mRNA Sample Prep Kit (protocol version: # 1000000124518 v02 (April 2021)) poly-A containing mRNA molecules were purified from the total RNA input using poly-dT oligo-attached magnetic beads. The purified mRNA was fragmented and in a reverse transcription reaction using random primers and Actinomycin D, RNA was converted into first strand cDNA and subsequently converted into double-stranded cDNA in a second strand cDNA synthesis reaction using dUTP to achieve strand specificity. The cDNA fragments were extended with a single 'A' base to the 3′ ends of the blunt-ended cDNA fragments after which pre-index anchors were ligated preparing the fragments for dual indexing. Anchor-ligated fragments were then purified using magnetic beads. Finally, enrichment PCR was carried out to enrich those DNA fragments that have anchor-ligated DNA fragments and to add indexes and primer sequences for cluster generation.

Sequencing

Purified dual-indexed sequence-libraries of each sample were equimolarly pooled and sequenced on Element Biosciences AVITI (2x75 Cloudbreak kit, single-end reads 100 (101-10-10-0)) at the VIB Nucleomics Core (https://nucleomicscore.sites.vib.be/en).

Preprocessing

Low quality ends and adapter sequences were trimmed off from the Illumina reads with FastX (RRID: SCR_005534) 0.0.14 [http://hannonlab.cshl.edu/fastx_toolkit/index.html] and Cutadapt (RRID: SCR_011841) 3.2.[95] Subsequently, small reads (length <35 bp), polyA-reads (more than 90% of the bases equal A), ambiguous reads (containing N), low-quality reads (more than 50% of the bases < Q25) and artifact reads (all but three bases in the read equal one base type) were filtered using using FastX 0.0.14 and ShortRead (RRID: SCR_006813) 1.58.0.[96] With Bowtie2 (RRID: SCR_016368) 2.4.5 we identified and removed reads that align to phix_illumina.[97]

Mapping

The preprocessed reads were aligned with STAR aligner (RRID: SCR_004463) v2.5.2b to the reference genome of Homo sapiens (GRCh38.88).[98] Default STAR aligner parameter settings were used, except for '–outSAMprimaryFlag OneBestScore –twopassMode Basic –alignIntronMin 50 –alignIntronMax 500000 –outSAMtype BAM SortedByCoordinate'. Using Samtools (RRID: SCR_002105) 1.15.1, reads with a mapping quality smaller than 20 were removed from the alignments.[99]

Counting

The number of reads in the alignments that overlap with gene features were counted with featureCounts (RRID: SCR_002105) 1.5.3.[100] Following parameters were chosen: -Q 0 -s 2 -t exon -g gene_id. We removed genes for which all samples had less than 1 count-per-million. Raw counts were further corrected within samples for GC-content and between samples using full quantile normalization, as implemented in the EDASeq (RRID: SCR_006751) 2.32 package from Bioconductor.[101]

Differential gene expression

With the EdgeR (RRID:SCR_012802) 3.42.4 package of Bioconductor, a negative binomial generalized linear model (GLM) was fitted against the normalized counts.[102] We did not use the normalized counts directly, but worked with offsets. Differential expression was tested for with a GLM likelihood ratio test, also implemented in the EdgeR package. The resulting *p*-values were corrected for multiple testing with Benjamini-Hochberg to control the false discovery rate.[112]

QUANTIFICATION AND STATISTICAL ANALYSIS

Statistical analysis was performed with Graphpad Prism (RRID:SCR_002798). Unpaired t test was used to compare innervated NMJs, blood vessel-positive area, number of GFAP positive, and GFAP and STING positive nuclei between *SOD1*^{G93A}/*Egln2*$^{-/-}$ and *SOD1*^{G93A}/*Egln2*$^{+/+}$ mice. One-way ANOVA with Dunnett's multiple comparison test was used to compare *Egln1*, *-2* and *-3* expression and, SOD1 expression between SOD1^{G93A}/*Egln2*$^{-/-}$, *SOD1*^{G93A}/*Egln2*$^{+/-}$ and *SOD1*^{G93A}/*Egln2*$^{+/+}$ mice, and *Stmn2* expression between different sizes of neuron area. One-way ANOVA with Tukey's multiple comparison test was used to compare disease duration between SOD1^{G93A}/*Egln2*$^{-/-}$, *SOD1*^{G93A}/*Egln2*$^{+/-}$, and *SOD1*^{G93A}/*Egln2*$^{+/+}$ mice. One-way ANOVA with Sidak's multiple comparison test was used to compare axonal length between zebrafish injected with control RNA (*SOD1*^{WT} or *GFP*), ALS RNA (*SOD1*^{G93A} or *C9orf72* sense repeats), and ALS RNA co-injected with control AMO or *egln2* AMO. Kruskal-Wallis test with Dunn's multiple comparison test was used to compare percentage of abnormal branching between zebrafish injected with control RNA (*SOD1*^{WT} or *GFP*), ALS RNA (*SOD1*^{G93A} or *C9orf72* sense repeats), and ALS RNA co-injected with control AMO or *egln2* AMO

and mRNA expression of *egln1a*, *egln1b*, *egln3*, and *vegfaa* between zebrafish injected with $SOD1^{WT}$, $SOD1^{G93A}$ and $SOD1^{G93A}$ co-injected with control AMO or *egln2* AMO zebrafish. Two-way ANOVA with Sidak's multiple comparison test was used to compare motor neuron count between $SOD1^{G93A}/Egln2^{-/-}$, and $SOD1^{G93A}/Egln2^{+/+}$ mice for different sizes of neuron area. Two-way ANOVA with Tukey's multiple comparison test was used to compare mRNA expression between $SOD1^{G93A}/Egln2^{-/-}$ and $SOD1^{G93A}/Egln2^{+/+}$ mice for different HIF targets. Log rank Mantel-Cox test was used to compare probability of disease onset and survival between $SOD1^{G93A}/Egln2^{-/-}$, $SOD1^{G93A}/Egln2^{+/-}$, and $SOD1^{G93A}/Egln2^{+/+}$ mice. *p*-values <0.05 were considered significant (*$p < 0.05$, **$p < 0.01$, ***$p < 0.001$, ****$p < 0.0001$). The data represent mean ± SEM with individual values shown. For each experiment, the definition and number of individual values (n) is provided in the figure legend.